

**Ab initio theory of phase stability and structural selectivity in Fe-Pd alloys**Roman V. Chepulsii,<sup>1,\*</sup> Sergey V. Barabash,<sup>2,†</sup> and Alex Zunger<sup>3</sup><sup>1</sup>*Department of Mechanical Engineering and Materials Science, Duke University, Durham, North Carolina 27708, USA*<sup>2</sup>*Department of Materials Science and Engineering, University of California at Los Angeles, Los Angeles, California 90095, USA*<sup>3</sup>*University of Colorado, Boulder, Colorado 80309, USA*

(Received 24 April 2011; revised manuscript received 13 September 2011; published 4 April 2012)

In Fe-Pd alloys, the competing geometric (fcc versus bcc) and magnetic tendencies result in rich phase stability and ordering physics. Here, we study these alloys via a first principles mixed-basis cluster expansion (CE) approach. Highly accurate fcc and bcc CEs are iteratively and self-consistently constructed using a genetic algorithm, based on the first principles results for  $\sim 100$  ordered structures. The structural and magnetic “filters” are introduced to determine whether a fully relaxed structure is of fcc/bcc and high-/low-spin types. All structures satisfying the Lifshitz condition for stability in extended phase diagram regions are included as inputs to our CEs. We find that in a wide composition range (with more than 1/3 atomic content of Fe), an fcc-constrained alloy has a single stable ordered compound, L1<sub>0</sub> FePd. However, L1<sub>0</sub> is higher in energy than the phase-separated mixture of bcc Fe and fcc-FePd<sub>2</sub> ( $\beta 2$  structure) at low temperatures. In the Pd-rich composition range, we find several fcc  $\beta 2$ -like ground states: FePd<sub>2</sub> ( $\beta 2$ ), Fe<sub>3</sub>Pd<sub>9</sub>, Fe<sub>2</sub>Pd<sub>7</sub>, FePd<sub>5</sub>, Fe<sub>2</sub>Pd<sub>13</sub>, and FePd<sub>8</sub>, yet we do *not* find FePd<sub>3</sub> with the experimentally observed L1<sub>2</sub> structure. Fcc Monte Carlo simulations show a transformation from any of the attempted  $\beta 2$ -like ground states directly into a disordered alloy. We suggest that the phonon and/or spin excitation contributions to the free energy are responsible for the observed stability of L1<sub>2</sub> at higher temperatures, and likely lead to a  $\beta 2 \leftrightarrow L1_2$  transition. Finally, we present here a complete characterization of all the fcc and bcc Lifshitz structures, i.e., the structures with ordering vectors exclusively at high-symmetry  $k$  points.

DOI: [10.1103/PhysRevB.85.144201](https://doi.org/10.1103/PhysRevB.85.144201)

PACS number(s): 61.66.Dk, 61.50.Ah, 81.05.Bx, 81.30.Bx

**I. INTRODUCTION**

Because of a large uniaxial magnetic anisotropy<sup>1</sup> and high resistance to corrosion, the L1<sub>0</sub>-FePd ferromagnetic compound is interesting as a hard magnetic material for ultrahigh density magnetic recording media.<sup>2</sup> Besides, Fe-Pd appears to be one of the most promising ferromagnetic shape memory alloys attractive for such practical multifunctional applications as rapid magnetic sensors and magneto-thermoelastic actuators due to the huge magnetic-field-induced strains.<sup>3</sup> Fe-Pd is also studied as a good catalytic system.<sup>4</sup>

Structurally, Fe-Pd is an interesting alloy system. Unlike the all-paramagnetic all-fcc (e.g., Cu-Au) or the all-bcc (e.g., Mo-Ta) alloys, Fe-Pd exhibits (see Fig. 1) a competition between bcc (Pd-poor and low-temperature) and fcc (Pd-rich and/or high-temperature) structures as well as an interplay between paramagnetic (high-temperature) and ferromagnetic (low-temperature) phases.<sup>6</sup> For example, with respect to magnetic ordering, inspection of Fig. 1 indicates four distinct regions in the phase diagram (the detailed discussion of the experimentally observed ordered Fe-Pd structures is presented in Ref. 7): (i) low-temperature ferromagnetic (FM) region containing fcc-FM and/or bcc-FM and (ii)–(iv) high-temperature regions above at least one of the Curie temperatures, containing the paramagnetic (PM) fcc-PM phase, either (ii) as the only component, or in equilibrium with (iii) bcc-FM or (iv) bcc-PM phases.

In our earlier work, see Ref. 7, the absolute (unrestricted) as well as fcc- and bcc-restricted ground-state structures obtained from first principles were briefly reported. In the present paper, we illustrate the diverse, fcc/bcc and high/low spin phase behavior of Fe-Pd from first principles (see Sec. II). It is shown that the results of Ref. 7 unambiguously follow from iteratively constructed first-principles mixed-basis cluster expansions

(see Secs. III and IV). New Fe-Pd ground states, all with Pd composition larger than equiatomic, are identified (see Fig. 7 and Appendix B). All these  $T = 0$  results belong to region (i) defined above. A proper analysis of phase equilibria in regions (ii)–(iv) could potentially require an explicit inclusion of the changes in the magnetic state that influence the finite temperature phase stability of Fe-containing systems.<sup>59,60</sup> One methodology previously attempted for such an analysis in Fe-containing alloys<sup>61</sup> involves a “disordered local moment” formalism. In the present paper, we do not attempt such an analysis, but instead address a related but more simple question: what would be the finite temperature ordering and phase stability in Fe-Pd alloys in the absence of magnetic excitations? We answer this question by combining our  $T = 0$  cluster expansion with Monte Carlo simulations, and comparing the results with experimental data (see Sec. V). These results give a first approximation for the ordering temperatures and finite- $T$  short-range signatures of the yet-unobserved phases predicted here and in Ref. 7. Further, our finite-temperature analysis demonstrates that the spin (or vibrational) excitations must be entirely responsible for the transition between the  $T = 0$  Fe<sub>3</sub>Pd<sub>9</sub> ordered structure predicted here and the high-temperature L1<sub>2</sub> ordered FePd<sub>3</sub> observed experimentally, and thus a detailed study of these effects is necessary to establish a true finite- $T$  phase stability in this system. Finally, we also present here a complete list of all the fcc and bcc Lifshitz structures, which correspond to high-symmetry  $k$  points (see Appendices C and D).

**II. EXISTENCE OF FCC/BCC PHASES AND HIGH-/LOW-SPIN CONFIGURATIONS**

The diverse phase behavior of Fe-Pd is illustrated by first-principles total energy calculations (see Sec. III E) for iron,

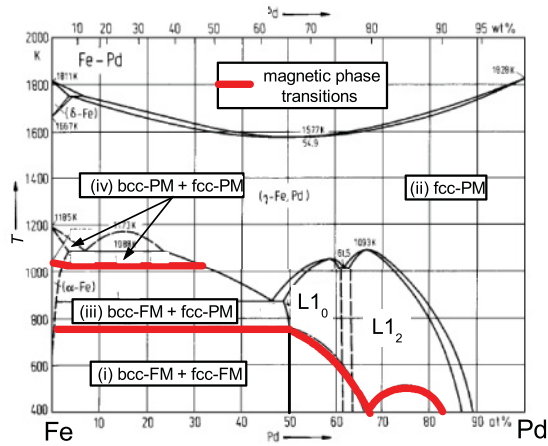


FIG. 1. (Color online) Measured (see Ref. 5) temperature-composition phase diagram of Fe-Pd. Four regions of different magnetic and structural configurations are marked. PM = paramagnetic and FM = ferromagnetic.

palladium and their compounds as a function of tetragonality  $c/a$  (see Fig. 2) and (collinear) magnetic moment (see Fig. 3). (To facilitate a comparison between structures with unit cells of different size and shape,  $c$  and  $a$  here refer to the lattice parameters in  $z$  and  $x, y$  directions, respectively, for a uniaxially distorted underlying fcc lattice.)

Figure 2 illustrates that as the palladium composition increases in Fe-Pd compounds, the position of the deepest global energy minimum along the Bain path tends to change from around the bcc ( $c/a = 1/\sqrt{2}$ ) geometry to around the fcc ( $c/a = 1$ ) geometry. Secondary minima can coexist with this global minimum: a secondary fct minimum coexists with a global bcc/bct minimum in pure Fe, and a secondary bct minimum coexists with a global fct/fcc minimum in  $\beta 1$ ,  $L1_0$ , and pure Pd. (We use “fct” or “bct” to refer to the tetragonal structures that are “fcc-based” or “bcc-based” as quantified below in Sec. III C; crystallographically, both have body-centered tetragonal symmetry.) A secondary minimum is locally stable only if any symmetry-unconstrained infinitesimal change in atomic positions increases its energy; such minima were reported in bcc K, Li, Rb, Sr, and in B2 CuZn (see Ref. 10). Frequently, a secondary minimum on a Bain path plot is locally unstable, because there exists an infinitesimal change in atomic positions (in the direction orthogonal to the Bain path) that decreases its energy; for example, such unstable secondary minima were reported for non-ground-state structure geometries of many elemental solids.<sup>10–13</sup> We find that the secondary (bct) minimum on the Bain path of  $\text{Fe}_2\text{Pd}-\beta 1$  [see Fig. 2(c)] is locally stable, while the fct minimum of Fe and the bct minima of Pd and  $L1_0$  FePd are locally unstable. We further find that the following fcc superlattices do not have secondary minima along the Bain path and all relax to bct structures: (001)  $\text{Fe}_3\text{Pd}$  (Z1), (011)  $\text{Fe}_3\text{Pd}$  (Y1), (111)  $\text{Fe}_3\text{Pd}$  (V1), (201)  $\text{Fe}_3\text{Pd}$  (DO<sub>22</sub>), (110)  $\text{Fe}_2\text{Pd}$  ( $\gamma 1$ ), (111)  $\text{Fe}_2\text{Pd}$  ( $\alpha 1$ ), and (111)  $\text{Fe}_2\text{Pd}_2$  (V2).

Even within the same geometry, Fe-Pd alloys may exhibit multiple minima depending on the total magnetic moment. Figure 3 shows that iron has a single global minimum corresponding to a high-spin bcc structure (HS-bcc), while in

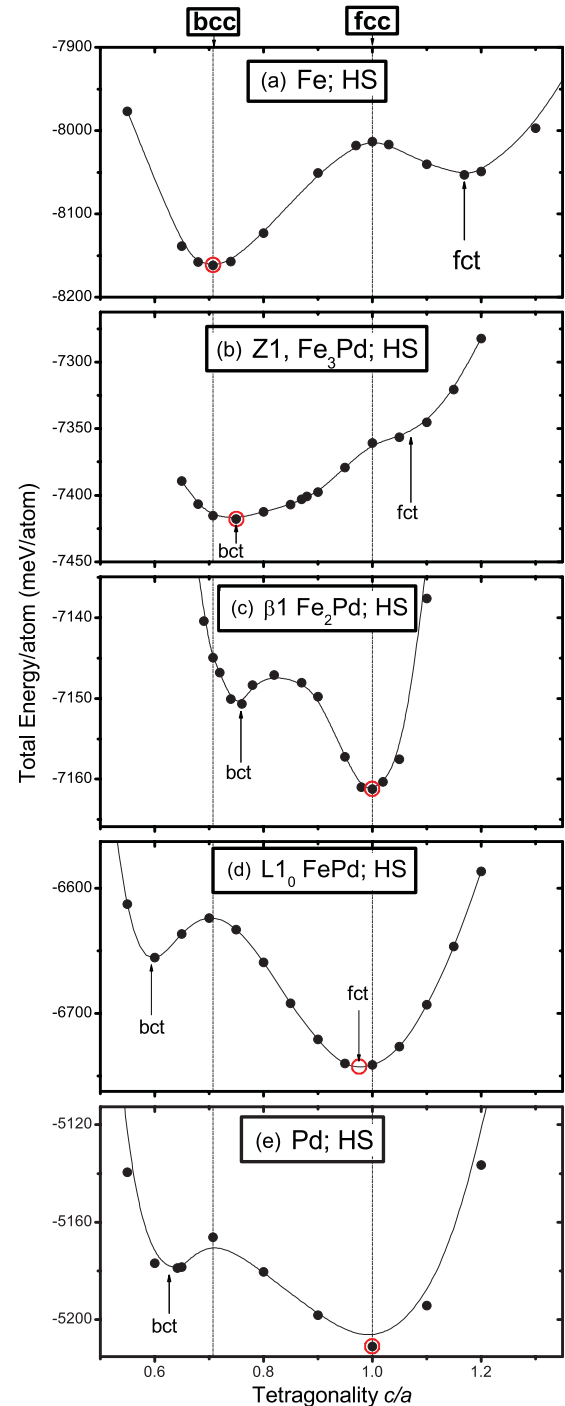


FIG. 2. (Color online) The dependence on the tetragonality ( $c/a$  ratio) of the total energy per atom for (a) high-spin (HS) iron, (b) (100)-fcc superlattice  $\text{Fe}_3\text{Pd}$  (Z1), (c) (100)-fcc superlattice  $\text{Fe}_2\text{Pd}$  ( $\beta 1$ ), (d) (100)-fcc superlattice  $\text{FePd}$   $L1_0$ , and (e) high-spin palladium. The unit cell shape is kept fixed for each  $c/a$  value and all other degrees of freedom are relaxed. Open (red) circles correspond to the global minima.

the fcc geometry it has *two* local minima: a higher-energy high-spin (HS-fcc) minimum and a lower-energy low-spin (LS-fcc) minimum.<sup>14</sup> For pure fcc palladium, our first-principles calculations predict the energy of the magnetic ground state to be  $\sim 1$  meV/atom lower than that of nonmagnetic state. As we

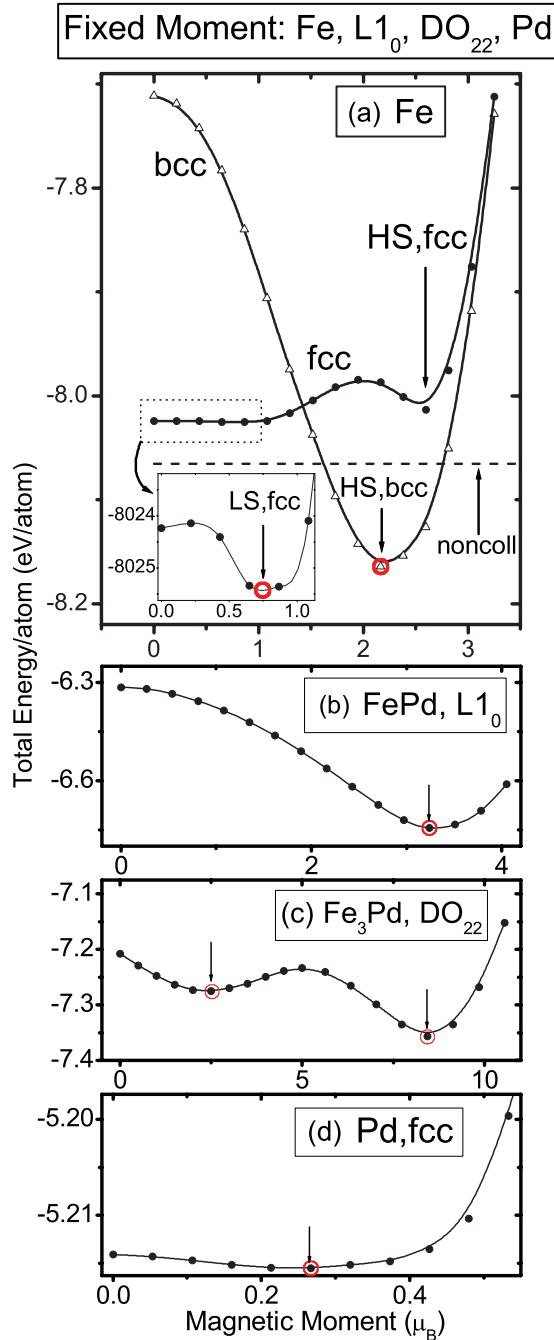


FIG. 3. (Color online) The dependence of the total energy on the (collinear) magnetic moment of the corresponding unit cell in (a) pure fcc and bcc iron, (b)  $L1_0$  (FePd), (c)  $DO_{22}$  ( $Fe_3Pd$ ), and (d) pure fcc palladium. The horizontal dashed line in (a) evaluates the lowest energy of noncollinear spin configuration of fcc iron calculated in Ref. 14. “HS” and “LS” denote high- and low-spin states, respectively. At each fixed magnetic moment, the structures are fully relaxed keeping the symmetry of unit cell fixed. Open (red) circles correspond to the global minima.

checked, the denser  $k$  mesh and higher energy cutoff do not change this conclusion. The magnetic ground state of Pd is not a consequence of pseudopotential usage as the published all-electron full-potential linearised augmented-plane wave (FLAPW)-generalized gradient approximation (GGA) results

are the same.<sup>15</sup> However, the magnetic versus nonmagnetic energy difference in Pd is comparable with the accepted accuracy of density functional theory (DFT) calculations in this paper thus having a negligible effect on all obtained results. A deep low-spin minimum exists in  $Fe_3Pd$   $DO_{22}$ ,<sup>16</sup> which is characterized by two Fe spins “up” and one “down” in the unit cell.

### III. METHODOLOGY

#### A. The cluster expansion strategy for systems exhibiting fcc/bcc phases and high-/low-spin configurations

Based on the above survey of a few fcc/bcc (see Fig. 2) and high-/low- spin phases (see Fig. 3), we conclude to perform the following distinct cluster expansions: (i) all-fcc (or fct) high-spin cluster expansion and (ii) all-bcc (or bct) high-spin cluster expansion. This allows us to describe the low-temperature ferromagnetic region containing fcc-FM and bcc-FM, i.e., part (i) of the phase diagram denoted in Sec. I and in Fig. 1. In both cases, we use only those structures that are at least locally stable within the corresponding Bravais lattice. This means that any input structure, or any structure that is suggested by the cluster expansion to be a candidate for a ground state, is relaxed without symmetry constrains. We implement fcc/bcc and HS/LS “filters” identifying the fully relaxed structures (see Secs. III C and III D). If a structure relaxes away from its initial reference lattice type, e.g., fcc, to another reference lattice type, e.g., bcc, then this structure is removed from the fcc cluster expansion. Similarly, we include only the structures in high-spin state as inputs to the cluster expansions.

#### B. The mixed-basis cluster expansion approach

We use the mixed-basis cluster expansion (MBCE) approach.<sup>17,19–21</sup> The formation energy of each structure  $\sigma$  based on a given crystal lattice (e.g., fcc or bcc) is mapped onto an Ising-like Hamiltonian:

$$\Delta H_{CE}(\sigma) = J_0 + (2x - 1)J_1 + \sum_{\text{pairs}}^{n_{\text{pairs}}} D_{\text{pair}} J_{\text{pair}} \bar{\Pi}_{\text{pair}}(\sigma) + \sum_f^{N_{\text{MB}}} D_f J_f \bar{\Pi}_f(\sigma), \quad (1)$$

where A and B type atoms are represented by pseudospins  $S = -1$  and  $S = +1$ , respectively,  $J_0$ ,  $J_1$ ,  $\{J_{\text{pair}}\}$  ( $n_{\text{pairs}}$  members) and  $\{J_f\}$  ( $N_{\text{MB}}$  members) are the atomic interaction coefficients,  $x$  is a composition,  $\bar{\Pi}_f(\sigma) = \frac{1}{ND_f} \sum_{(i_1, i_2, \dots, i_m) \sim f} S_{i_1}(\sigma) S_{i_2}(\sigma) \dots S_{i_m}(\sigma)$  are geometric factors describing configuration  $\sigma$ ,  $D_{\text{pair}}$ , and  $D_f$  are the numbers of symmetrically equivalent pairs and nonpairs corresponding to a given interaction. The atomic interactions  $J$ s are determined by fitting  $\Delta H_{CE}(\sigma)$  to the formation energies  $\Delta H_{DFT}(\sigma)$  obtained from first principles for some finite number of structures. After the  $J$ s are known, the formation energy  $\Delta H_{CE}(\sigma)$  for any structure  $\sigma$  can be easily obtained by using Eq. (1).

Note that the formation energies that are used for the lattice-specific cluster expansions (as presented in Appendix B or in Fig. 8 below), are defined with respect to the pure elements in the respective geometry, despite the local instability of fcc Fe and bcc Pd. We find that using fct Fe instead of fcc Fe does not

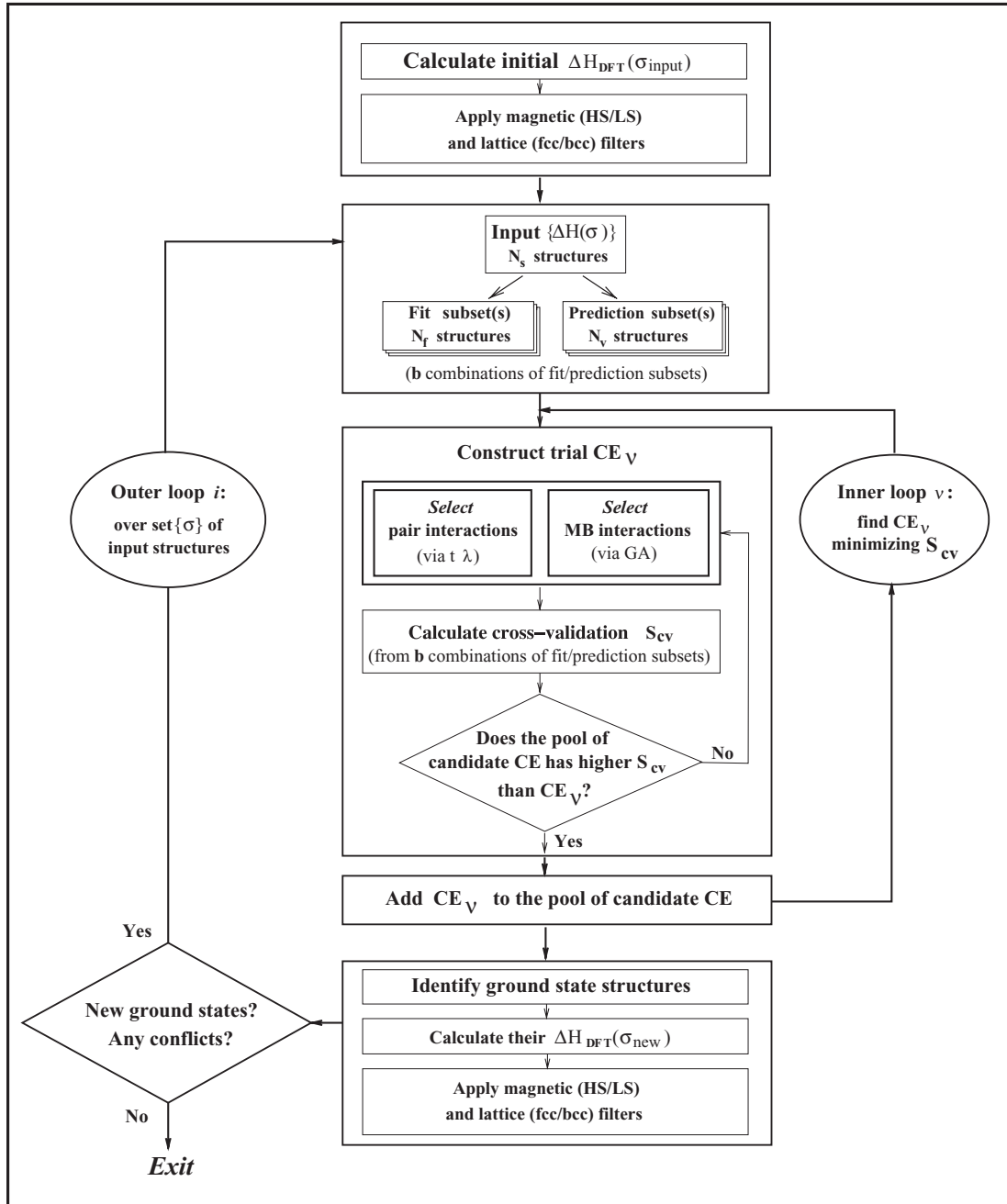


FIG. 4. Flowchart of the iterative procedure used to establish the self-consistent cluster expansion, where GA is a genetic algorithm, CE is a cluster expansion, and  $S_{CV}$  is a cross-validation score. The flowchart is modified with respect to the Fig. 3 in Ref. 21 by inclusion of the fcc/bcc and HS/LS filters for DFT inputs as explained in Secs. III C and III D, respectively.

change the cluster expansion results qualitatively. Whenever the results of the two cluster expansions are combined to determine the global ground states (e.g., in Fig. 7), we redefine the formation energies with respect to bcc Fe and fcc Pd, as relevant experimentally.

To find the  $J$ s, we apply the procedure developed and described in detail in Ref. 21 (as summarized below). We further modify this procedure by including fcc/bcc and HS/LS filters for DFT inputs, as explained in Secs. III C and III D, respectively. The flowchart of the procedure is presented in Fig. 4. We start from an initial set of input structures for which

we calculate their formation energies  $\{\Delta H_{DFT}(\sigma)\}$  and apply the fcc/bcc and HS/LS filters. The set is divided into two groups:  $N_f$  structures used to extract  $J$ s by fitting  $\Delta H_{DFT}(\sigma)$  to  $\Delta H_{CE}(\sigma)$  and  $N_v$  structures used for testing the cluster expansion predictions. The “inner” loop searches for  $J$ s corresponding to a fixed set of input structures  $\{\Delta H_{DFT}(\sigma)\}$ . This is done by a reciprocal space fit for pair interactions using a constrained minimization (“ $t - \lambda$ ” procedure,<sup>17,18</sup> see further discussion of this procedure applied to Fe-Pd in Sec. IX of Supplemental Material<sup>55</sup>). For optimal determination of nonpair many-body interactions (MBITs), we use a genetic

algorithm, as described in Refs. 19 and 20. The selection of pairs and MBITs is judged by a minimization of the prediction error called “leave-many-out” cross-validation score<sup>22</sup>  $S_{CV}$ .

The inner loop creates a pool of cluster expansions that have the lowest cross-validation scores. The ground states of such cluster expansions are found from Eq. (1) searching all possible structures (with all possible inequivalent unit cell shapes) with up to 20 atoms per unit cell,<sup>56</sup> i.e.,  $\sim 2^{20}$  structures. These ground states are statistically ranked by “depth” (relative to the corresponding convex hulls) and “frequency” of appearance. Only the “deep” ( $>1$  meV/atom) and “frequent” ( $>30\%$ ) ground states are chosen for subsequent DFT verification. Such statistical analysis diminishes the risk of cross-validation score overoptimization<sup>22</sup> while ensuring that only the energy differences exceeding the accuracy of the first principles inputs ( $\sim 1$  meV/atom, cf. Sec. III E below) are given full attention.

DFT calculation without symmetry constrains is performed for each of the so-chosen “predicted” ground states. Then, we check if this prediction is (1) fcc or bcc “locally stable” high-spin, and (2) “confirmed” or “refuted” by DFT (i.e., whether it belongs to the DFT convex hull). If we find some “locally stable” high-spin structure(s) being “confirmed by DFT” we (3) note if some ground states found at previous iterations are now “removed from DFT convex hull.” At each outer loop iteration, we add all of the “new” (comparing to previous iterations) ground-state predictions, both correct and incorrect (but locally stable and high-spin), to the DFT input set for the next iteration, thereby increasing this set.

The outer loop iterations are deemed converged when no new, high-spin, and locally stable ground states are predicted by the cluster expansions. Tables I and II illustrate the convergence of outer loop iterations for fcc and bcc Fe-Pd. For example, in the fcc case, at the fifth iteration (IT = 5), we have 12 ground-state predictions, of which six are DFT confirmed, three are DFT refuted, and three are found to be locally fcc unstable. Among nine fcc locally stable ground-state predictions, only three are found as “new” comparing to previous iterations. So for the next iteration (IT = 6), we have three more DFT inputs.

It has been shown before<sup>17,23</sup> that the short-range cluster expansion can not predict correctly the formation energies of strained long-period  $A_nB_n$  superlattices. Indeed, the energy of any such a superlattice in the limit of  $n \rightarrow \infty$  is the sum of the energies of strained A + B, and thus depends on the superlattice orientation  $\hat{G}$ . However, the atoms separated by a distance longer than the cluster expansion interaction range do not interact within such cluster expansion. Therefore a short-range cluster expansion predicts the  $n \rightarrow \infty$  energy to be zero, regardless of the superlattice orientation. For elastically locally stable systems, the obvious solution is to calculate the elastic energy  $E_{CS}(\hat{G})$  for each orientation  $\hat{G}$  and subtract it from  $E_{CE}(\sigma)$  (for  $\sigma$  having a nonzero structure factor in direction  $\hat{G}$ ) and then perform the cluster expansion for energies  $E_{CE}(\sigma) - E_{CS}(\hat{G})$ . The so-obtained cluster expansion converges well and the subsequent adding of  $E_{CS}(\hat{G})$  to  $E_{CE}(\sigma)$  guaranties the correct asymptotical behavior of the total energy. Unfortunately, Fe-Pd is elastically unstable. If we formally perform calculation of  $E_{CS}(\hat{G})$  in Fe-Pd, we obtain the negative values: for some directions [e.g., (100) and (301)]

at all compositions and for other directions [e.g., (201) and (311)] at low palladium compositions. The negative values of constituent strain energies are the consequence of the well-known dynamical instability of the HS fcc Fe, which can relax without a barrier into the more energetically favorable HS bcc Fe, as can be clearly seen from Fig. 2(a). The mismatch between the smaller HS Fe ( $a = 3.64$  Å) and the larger Pd ( $a = 3.96$  Å) atoms leads to a decreased  $c/a$  and an elastic energy lowering in (100) fcc superlattices, which in sufficiently Fe-rich structures could lead to a barrierless transformation to a bcc-like structure; indeed, our results below confirm such a prediction. In the present work, we do not add/subtract  $E_{CS}(\hat{G})$  from/to  $E_{CE}(\sigma)$ . This means that we can not use our cluster expansion for long-period superlattices. In practice, our cluster expansion works for periods  $n \leq 4$ , as verified by fits (see Appendix B). The long-period superlattices have not been observed in Fe-Pd experimentally and, during cluster expansion iterations, we have not obtained them as ground-state predictions. The formal inclusion of constituent strain into a number of cluster expansion iterations did not reveal new valid ground-state predictions but rather some additional spurious ones.

### C. Determination of the fcc and bcc degrees for structures

In order to determine whether a given relaxed structure is bcc- or fcc like, we calculate and compare the corresponding degrees based on the relaxed atomic positions. We define the degree  $s^{(\alpha)}(\sigma)$  of proximity of a given structure  $\sigma$  to the underlying lattice type  $\alpha$  ( $\alpha = \text{fcc, bcc, sc}$ ) as

$$s^{(\alpha)}(\sigma)^{-1} = \sum_{i=1, \dots, N} \sum_{j \neq i} [d_{ij}(\sigma) - d_{ij}(\alpha)]^2 \exp[-\eta d_{ij}(\alpha)]. \quad (2)$$

Here, the first sum runs over the atoms  $i = 1, \dots, N$  in the basis of the structure, the second sum runs over all atoms  $j$  in the lattice (in order to limit this sum to a finite portion of the lattice, an exponential decay parameter  $\eta \sim 1$  is introduced), and  $d_{ij}$  is the dimensionless interatomic distance between atoms  $i$  and  $j$  normalized by the cube root of the volume per atom. To determine the correspondence between the interatomic distances  $d_{ij}(\sigma)$  of the relaxed structure  $\sigma$  and those of a perfect lattice  $\alpha$ , we sort the distances  $\{d_{ij}(\sigma)\}$  in increasing order (which is done separately for each atom  $i$  in the basis) and then match them to the similarly sorted distances in the perfect lattice. For example, if  $\alpha = \text{fcc}$ , then for each  $i$  the twelve shortest  $d_{ij}(\sigma)$ 's would be matched to the nearest-neighbor distance  $d_{nn}(\text{fcc})$ , while the next six  $d_{ij}(\sigma)$ 's would be matched to the second-nearest-neighbor distance  $d_{n2n}(\text{fcc})$ , etc. If, for example, the degree  $s^{\text{fcc}}(\sigma)$  for a given relaxed structure  $\sigma$  is much larger than alternative  $s^{\text{bcc}}(\sigma)$  and  $s^{\text{sc}}(\sigma)$  degrees, we conclude that it has relaxed to an fcc-like geometry. In case when there is no one structural degree  $s^{(\alpha)}(\sigma)$  clearly prevailing over the two others, the corresponding structure is not included into any of the cluster expansions.

Figure 5 illustrates this selection process for (011)  $\text{Fe}_2\text{Pd}$  ( $\gamma 1$ ) and (011)  $\text{Fe}_2\text{Pd}_2$  ( $Y 2$ ) superlattices. All of the interatomic distances  $d_{ij}$  are shown for the relaxed structures as well as for the perfect reference fcc and bcc lattices. The correspondence of the interatomic distances of a given relaxed

TABLE I. Outer-loop iteration history for high-spin fcc Fe-Pd cluster expansion. “DFT convex hull” means the ground states determined within the set of all those  $N_{\text{DFT}}$  structures for which DFT formation energies are known at each iteration step.  $N_{\text{mb}}^{\text{max}}$  is the maximum number of many-body interactions used for evaluation of cluster expansion predictions. The formation energies and description of all considered structures are presented in Appendices B–D<sup>43–47</sup> and in Supplemental Material (see Ref. 55).

<b>Fe-Pd fcc FM Cluster Expansion: Iteration History (seven final DFT ground states<sup>(a)</sup>)</b>										
	Input	IT = 1	IT = 2	IT = 3	IT = 4	IT = 5	IT = 6	IT = 7	IT = 8	IT = 9
$N_{\text{DFT}}$	29	29	40	49	63	71	75	76	80	83
$N_{\text{mb}}^{\text{max}}$		9	10	9	8	8	7	6	8	8
Total ground states predicted by cluster expansions		13	13	18	12	12	10	8	9	7
Correct (confirmed by DFT)		5 <sup>(b1)</sup>	4 <sup>(b2)</sup>	2 <sup>(b3)</sup>	4 <sup>(b4)</sup>	6 <sup>(b5)</sup>	5 <sup>(b6)</sup>	5 <sup>(b7)</sup>	5 <sup>(b8)</sup>	5 <sup>(b8)</sup>
Incorrect (refuted by DFT)		7 <sup>(c1)</sup>	7 <sup>(c2)</sup>	14 <sup>(c3)</sup>	8 <sup>(c4)</sup>	3 <sup>(c5)</sup>	2 <sup>(c6)</sup>	3 <sup>(c7)</sup>	2 <sup>(c8)</sup>	0
fcc-unstable in DFT		1 <sup>(d1)</sup>	2 <sup>(d2)</sup>	2 <sup>(d3)</sup>	0	3 <sup>(d5)</sup>	3 <sup>(d6)</sup>	0	2 <sup>(d8)</sup>	2 <sup>(d9)</sup>
New fcc locally stable (incl. shallow)		11	9	14	8	3	1	4	3	0
DFT convex hull	4 <sup>(e0)</sup>	6 <sup>(e1)</sup>	6 <sup>(e2)</sup>	6 <sup>(e2)</sup>	6 <sup>(e2)</sup>	6 <sup>(e2)</sup>	6 <sup>(e2)</sup>	7 <sup>(e7)</sup>	7 <sup>(e7)</sup>	7 <sup>(e7)</sup>
Structures removed from DFT convex hull		1	2	0	0	0	0	0	0	0
Cross-validation score (meV)		2	1.5	3	4	4	4.5	4	5	5
<b>Final DFT ground states:</b>										
(a) L1 <sub>0</sub> , $\beta$ 2, Fe <sub>3</sub> Pd <sub>9</sub> (ID-4748), Fe <sub>2</sub> Pd <sub>7</sub> (ID-580), FePd <sub>5</sub> (ID-67), Fe <sub>2</sub> Pd <sub>13</sub> (ID-30073), FePd <sub>8</sub> (ID-579)										
<b>Correct predictions:</b>										
(b1)	$\beta$ 2, DO <sub>23</sub> ,	FePd <sub>5</sub> (ID-67), FePd <sub>7</sub> (ID-279), FePd <sub>14</sub> (ID-28503)								
(b2)	$\beta$ 2,	Fe <sub>2</sub> Pd <sub>7</sub> (ID-580),	Fe <sub>2</sub> Pd <sub>13</sub> (ID-30073), FePd <sub>8</sub> (ID-579)							
(b3)	$\beta$ 2,	FePd <sub>8</sub> (ID-579)								
(b4)	$\beta$ 2,	FePd <sub>5</sub> (ID-67), Fe <sub>2</sub> Pd <sub>13</sub> (ID-30073), FePd <sub>8</sub> (ID-579)								
(b5)	L1 <sub>0</sub> , $\beta$ 2,	Fe <sub>2</sub> Pd <sub>7</sub> (ID-580), FePd <sub>5</sub> (ID-67), Fe <sub>2</sub> Pd <sub>13</sub> (ID-30073), FePd <sub>8</sub> (ID-579)								
(b6)	L1 <sub>0</sub> , $\beta$ 2,	FePd <sub>5</sub> (ID-67), Fe <sub>2</sub> Pd <sub>13</sub> (ID-30073), FePd <sub>8</sub> (ID-579)								
(b7)	L1 <sub>0</sub> , $\beta$ 2, Fe <sub>3</sub> Pd <sub>9</sub> (ID-4748),	FePd <sub>5</sub> (ID-67),			FePd <sub>8</sub> (ID-579)					
(b8)	L1 <sub>0</sub> , $\beta$ 2,	Fe <sub>2</sub> Pd <sub>7</sub> (ID-580), FePd <sub>5</sub> (ID-67),			FePd <sub>8</sub> (ID-579)					
<b>Incorrect predictions:</b>										
(c1) Fe <sub>5</sub> Pd <sub>4</sub> (ID-585), Fe <sub>5</sub> Pd <sub>4</sub> (ID-588), Fe <sub>4</sub> Pd <sub>4</sub> (ID-289), Fe <sub>4</sub> Pd <sub>5</sub> (ID-585), Fe <sub>2</sub> Pd <sub>3</sub> (ID-20), Fe <sub>3</sub> Pd <sub>13</sub> (ID-64323), FePd <sub>7</sub> (ID-290)										
(c2) Fe <sub>4</sub> Pd <sub>5</sub> (ID-588), Fe <sub>4</sub> Pd <sub>5</sub> (ID-627), Fe <sub>2</sub> Pd <sub>7</sub> (ID-583), Fe <sub>2</sub> Pd <sub>8</sub> (ID-1092), Fe <sub>3</sub> Pd <sub>12</sub> (ID-30123), FePd <sub>7</sub> (ID-290), FePd <sub>8</sub> (ID-502)										
(c3) Fe <sub>10</sub> Pd <sub>6</sub> (ID-91210), Fe <sub>8</sub> Pd <sub>8</sub> (ID-91218), Fe <sub>7</sub> Pd <sub>9</sub> (ID-91235), Fe <sub>4</sub> Pd <sub>10</sub> (ID-16161), Fe <sub>4</sub> Pd <sub>12</sub> (ID-63521), Fe <sub>2</sub> Pd <sub>6</sub> (ID-342), Fe <sub>2</sub> Pd <sub>6</sub> (ID-211), Fe <sub>2</sub> Pd <sub>8</sub> (ID-1133), FePd <sub>4</sub> (ID-30), Fe <sub>2</sub> Pd <sub>10</sub> (ID-4830), Fe <sub>2</sub> Pd <sub>11</sub> (ID-7900), Fe <sub>2</sub> Pd <sub>14</sub> (ID-91276), FePd <sub>9</sub> (ID-1132), FePd <sub>13</sub> (ID-15787)										
(c4) Fe <sub>4</sub> Pd <sub>4</sub> (ID-286), Fe <sub>4</sub> Pd <sub>4</sub> (ID-303), Fe <sub>4</sub> Pd <sub>4</sub> (ID-307), Fe <sub>3</sub> Pd <sub>4</sub> (ID-112), Fe <sub>3</sub> Pd <sub>4</sub> (ID-129), Fe <sub>4</sub> Pd <sub>7</sub> (ID-1852), Fe <sub>2</sub> Pd <sub>6</sub> (ID-300), Fe <sub>2</sub> Pd <sub>7</sub> (ID-541)										
(c5) Fe <sub>3</sub> Pd <sub>2</sub> (ID-23), Fe <sub>4</sub> Pd <sub>11</sub> (ID-36312), Fe <sub>2</sub> Pd <sub>7</sub> (ID-541)										
(c6) Fe <sub>2</sub> Pd <sub>7</sub> (ID-541), Fe <sub>3</sub> Pd <sub>12</sub> (ID-28042)										
(c7) Fe <sub>6</sub> Pd <sub>6</sub> (ID-3258), Fe <sub>3</sub> Pd <sub>13</sub> (ID-63086), FePd <sub>7</sub> (ID-269)										
(c8) Fe <sub>6</sub> Pd <sub>2</sub> (ID-211), Fe <sub>2</sub> Pd <sub>10</sub> (ID-6068)										
<b>fcc-unstable predictions:</b>										
(d1) Fe <sub>7</sub> Pd <sub>2</sub> (ID-580)					(d6) Fe <sub>6</sub> Pd(ID-106), Fe <sub>5</sub> Pd <sub>2</sub> (ID-91), Fe <sub>5</sub> Pd <sub>2</sub> (ID-107)					
(d2) Y1, $\gamma$ 1					(d8) Fe <sub>4</sub> Pd <sub>2</sub> (ID-39), Fe <sub>3</sub> Pd <sub>2</sub> (ID-19)					
(d3) Fe <sub>7</sub> Pd(ID-290), Y1					(d9) Fe <sub>6</sub> Pd <sub>2</sub> (ID-135), Fe <sub>3</sub> Pd <sub>2</sub> (ID-19)					
(d5) Fe <sub>6</sub> Pd(ID-106), Fe <sub>5</sub> Pd <sub>2</sub> (ID-91), Fe <sub>3</sub> Pd <sub>2</sub> (ID-19)										
<b>DFT convex hull:</b>										
(e0) L1 <sub>0</sub> , $\beta$ 2, DO <sub>23</sub> , D7										
(e1) L1 <sub>0</sub> , $\beta$ 2, DO <sub>23</sub> ,										
FePd <sub>5</sub> (ID-67), FePd <sub>7</sub> (ID-279), FePd <sub>14</sub> (ID-28503)										
(e2) L1 <sub>0</sub> , $\beta$ 2,										
Fe <sub>2</sub> Pd <sub>7</sub> (ID-580), FePd <sub>5</sub> (ID-67), Fe <sub>2</sub> Pd <sub>13</sub> (ID-30073), FePd <sub>8</sub> (ID-579)										
(e7) L1 <sub>0</sub> , $\beta$ 2, Fe <sub>3</sub> Pd <sub>9</sub> (ID-4748), Fe <sub>2</sub> Pd <sub>7</sub> (ID-580), FePd <sub>5</sub> (ID-67), Fe <sub>2</sub> Pd <sub>13</sub> (ID-30073), FePd <sub>8</sub> (ID-579)										

structure to those of the perfect lattices are consistent with the degrees  $s^{(\alpha)}(\sigma)$  (shown in the insert in the same figure). Note that because the different sites in the unit cell basis can be symmetry inequivalent, two or more interatomic distances (points in Fig. 5) may correspond to the same absolute neighbor number.

Following the above-described procedure, we find, for example, that among all 29 fcc compounds from the initial set, seven superlattices [(001) Fe<sub>3</sub>Pd (Z1), (011) Fe<sub>3</sub>Pd (Y1), (111) Fe<sub>3</sub>Pd (V1), (201) Fe<sub>3</sub>Pd (DO<sub>22</sub>), (110) Fe<sub>2</sub>Pd ( $\gamma$ 1), (111) Fe<sub>2</sub>Pd ( $\alpha$ 1), and (111) Fe<sub>2</sub>Pd<sub>2</sub> (V2)] have relaxed into bct structures, and thus are removed from the fcc cluster expansion.

TABLE II. The same as in Table I but for bcc.

Fe-Pd bcc FM Cluster Expansion: Iteration History (two final DFT ground states <sup>(a)</sup> )						
	Input	IT = 1	IT = 2	IT = 3	IT = 4	IT = 5
$N_{\text{DFT}}$	23	23	28	30	31	32
$N_{\text{mb}}^{\text{max}}$		8	8	7	7	8
Total ground states predicted by cluster expansions		10	7	10	11	12
Correct (confirmed by DFT)		2 <sup>(b1)</sup>	0	2 <sup>(b1)</sup>	1 <sup>(b4)</sup>	2 <sup>(b1)</sup>
Incorrect (refuted by DFT)		4 <sup>(c1)</sup>	2 <sup>(c2)</sup>	1 <sup>(c3)</sup>	1 <sup>(c4)</sup>	0
bcc-unstable in DFT		4 <sup>(d1)</sup>	5 <sup>(d2)</sup>	7 <sup>(d3)</sup>	9 <sup>(d4)</sup>	10 <sup>(d5)</sup>
New predictions that are bcc locally stable (including shallow)		5	2	1	1	0
DFT convex hull	1 <sup>(e0)</sup>	2 <sup>(e1)</sup>				
Structures removed from DFT convex hull		0	0	0	0	0
Cross-validation score (meV)		3	3.5	6	7.5	6.5
<b>Final DFT ground states:</b>						
(a) C11b, FePd <sub>8</sub> (ID-619)						
<b>Correct predictions:</b>						
(b1) C11b, FePd <sub>8</sub> (ID-619)      (b4) C11b						
<b>Incorrect predictions:</b>						
(c1) Fe <sub>4</sub> Pd <sub>4</sub> (ID-246), Fe <sub>2</sub> Pd <sub>7</sub> (ID-578), FePd <sub>4</sub> (ID-29), FePd <sub>5</sub> (ID-77)      (c3) Fe <sub>2</sub> Pd <sub>7</sub> (ID-622)						
(c2) Fe <sub>2</sub> Pd <sub>14</sub> (ID-90944), FePd <sub>15</sub> (ID-90943)      (c4) Fe <sub>5</sub> Pd <sub>4</sub> (ID-520)						
<b>Bcc-unstable predictions:</b>						
(d1) B11, Fe <sub>2</sub> Pd <sub>4</sub> (ID-48), Fe <sub>2</sub> Pd <sub>7</sub> (ID-569), FePd <sub>4</sub> (ID-24)						
(d2) Fe <sub>4</sub> Pd <sub>8</sub> (ID-3264), Fe <sub>4</sub> Pd <sub>8</sub> (ID-3239), Fe <sub>2</sub> Pd <sub>6</sub> (ID-269), Fe <sub>2</sub> Pd <sub>6</sub> (ID-240), FePd <sub>4</sub> (ID-27)						
(d3) Fe <sub>7</sub> Pd <sub>8</sub> (ID-36367), Fe <sub>2</sub> Pd <sub>4</sub> (ID-48), FePd <sub>4</sub> (ID-24), FePd <sub>4</sub> (ID-27), FePd <sub>5</sub> (ID-67), FePd <sub>8</sub> (ID-563), FePd <sub>9</sub> (ID-963)						
(d4) Fe <sub>2</sub> Pd <sub>4</sub> (ID-53), Fe <sub>2</sub> Pd <sub>4</sub> (ID-48), Fe <sub>2</sub> Pd <sub>7</sub> (ID-525), FePd <sub>4</sub> (ID-24), FePd <sub>4</sub> (ID-27), FePd <sub>8</sub> (ID-542), FePd <sub>8</sub> (ID-521), FePd <sub>8</sub> (ID-490), FePd <sub>9</sub> (ID-963)						
(d5) Fe <sub>5</sub> Pd <sub>4</sub> (ID-517), Fe <sub>5</sub> Pd <sub>4</sub> (ID-501), Fe <sub>4</sub> Pd <sub>4</sub> (ID-256), Fe <sub>2</sub> Pd <sub>6</sub> (ID-269), Fe <sub>2</sub> Pd <sub>7</sub> (ID-525), FePd <sub>4</sub> (ID-27), FePd <sub>5</sub> (ID-72), Fe <sub>2</sub> Pd <sub>14</sub> (ID-91778), FePd <sub>8</sub> (ID-542), FePd <sub>8</sub> (ID-563)						
<b>DFT convex hull:</b>						
(e0) C11b      (e1) C11b, FePd <sub>8</sub> (ID-619)						

#### D. Filtering of the high- and low-spin phases

Before the bulk of our study, we perform a number of test calculations including those shown in Fig. 3, so as to later be able to judge the magnetic state of any given relaxed structure. First, we analyze the correlation between the total magnetic moment  $\mu$  and composition  $x_{\text{Pd}}$  for a large number of key compounds. Second, for each of a smaller number of

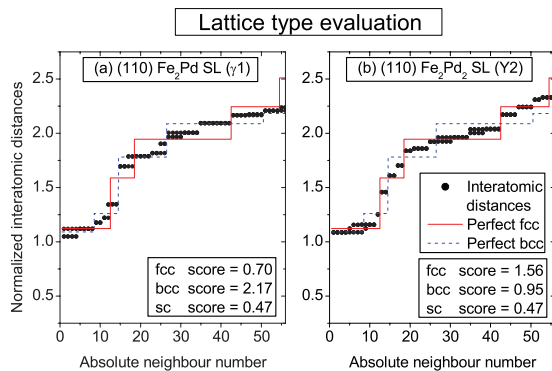


FIG. 5. (Color online) Interatomic distance analysis for (a) (110) Fe<sub>2</sub>Pd superlattice  $\gamma 1$  and (b) (110) Fe<sub>2</sub>Pd<sub>2</sub> superlattice Y2 (dots) with respect to those distances in the perfect fcc (solid lines) and bcc (dashed lines) lattices. The “fcc/bcc/sc scores” are the corresponding values of the degree  $s^{(\alpha)}(\sigma)$  defined in Eq. (2).

compounds, we perform a series of fixed moment calculations ( $\mu$  scans). From both sets of tests, we conclude that the total moments of the HS phases (excluding the pure elements) are well approximated linearly as  $\mu \sim (2.65x_{\text{Fe}} + 0.5x_{\text{Pd}})N \pm 0.3$  (where  $N$  is the total number of atoms). Thus it can be partitioned into individual contributions of roughly  $\mu_{\text{Fe}} \sim 2.65$  and  $\mu_{\text{Pd}} \sim 0.5$ . Due to much more limited occurrence of LS minima (in particular, LS was not observed in compounds with  $x_{\text{Pd}} > 0.5$ ), the magnetic moments of the LS compounds could not be partitioned with a similar certainty, but are consistent with  $\mu_{\text{Fe}} < 1.3$  and  $\mu_{\text{Pd}} \sim 0.5$ . Note that, as Figs. 3(a) and 3(d) illustrate, the LS and HS states are typically well separated whenever the LS state is clearly discernible.

For other structures in our HS cluster expansion study, we use these results as a benchmark. We check the total magnetization  $\mu$  of a relaxed structure and label the structure as being in a given spin state if  $\mu$  agrees well with the expected value of that spin state. Such a strategy proves its effectiveness for all the considered structures. We find that the HS magnetic state has a very robust value across all the CE inputs, as illustrated in Ref. 55.

#### E. Calculation of formation energies

We calculate the formation energies of Fe-Pd compounds using the pseudopotential momentum-space total energy and force formalism within the plane-augmented-wave (PAW)

method in DFT-GGA approximation of Perdew and Wang<sup>25</sup> with parametrization of Vosko, Wilk, and Nusair<sup>26</sup> as implemented by the VASP program package.<sup>27</sup>  $3p$  electrons are considered as valence for Fe. All calculations are spin polarized. The effect of lattice vibrations is omitted. All structures are completely relaxed including shape and volume relaxation of the unit cell as well as the individual displacements of atoms within the unit cell. The relaxation is symmetry unconstrained. The accuracy of relaxation is estimated at 1 meV/atom in terms of the total energy per atom for each compound.

In Supplemental Material,<sup>55</sup> we demonstrate the convergence of the calculated formation energies with respect to the  $k$  mesh and energy cutoff parameters. Based on the results of this test, we use the energy cutoff as 400 eV and  $k$  mesh equivalent to at least  $16 \times 16 \times 16$  divisions of the fcc and  $20 \times 20 \times 20$  divisions of the bcc cubic unit cells. In Appendix A, we compare our pseudopotential data with all-electron linearised augmented-plane wave (LAPW) and experimental data<sup>28–42</sup> for pure iron and palladium as well as for some of their compounds.

The results of our first-principles calculations of the formation energies  $\Delta H$  of fcc and bcc compounds are presented in Appendix B. The energies of all locally stable inequivalent structures with four or less atoms per unit cell are included into the first input set. Additionally, all fcc and bcc Lifshitz structures, which correspond to high-symmetry  $k$  points, are considered. Since such Lifshitz structures have never been

compiled together,<sup>43–47</sup> we list them in Appendices C and D. For fcc cluster expansion, we also use the energy of  $D0_{23}$  structures because it has very low  $\Delta H$ . Thus the total number of the *initial* DFT inputs consists of 30 fcc and 23 bcc energies (including pure iron and palladium). The *total* pool of the DFT inputs, including the initial set and the structures added during the iterations of the cluster expansion, consists of 83 fcc and 32 bcc energies.

## IV. RESULTS OF THE CLUSTER EXPANSIONS

### A. Interaction energies in fcc and bcc Fe-Pd

Figure 6 shows the interaction energies that characterize the calculated fcc and bcc cluster expansions. The fcc cluster expansion yields two strong and 12 weaker pair interactions, whereas the bcc cluster expansion yields five strong and six weaker pair interactions. The strong pair interactions are ordering-like (positive) in fcc but in bcc they are ordering-like (positive) for 1st, 3rd, and 5th pair and phase-separating (negative) for 2nd and 4th pairs. The same tendency is observed among the many-body interactions. Namely, in fcc, all of them, except 4B3-2 are ordering like, whereas in bcc, they are both ordering like and phase separating.

### B. Convergence of the cluster expansion iterations

Tables I and II show the iterative convergence of the fcc and bcc cluster expansions toward self-consistency. In case of

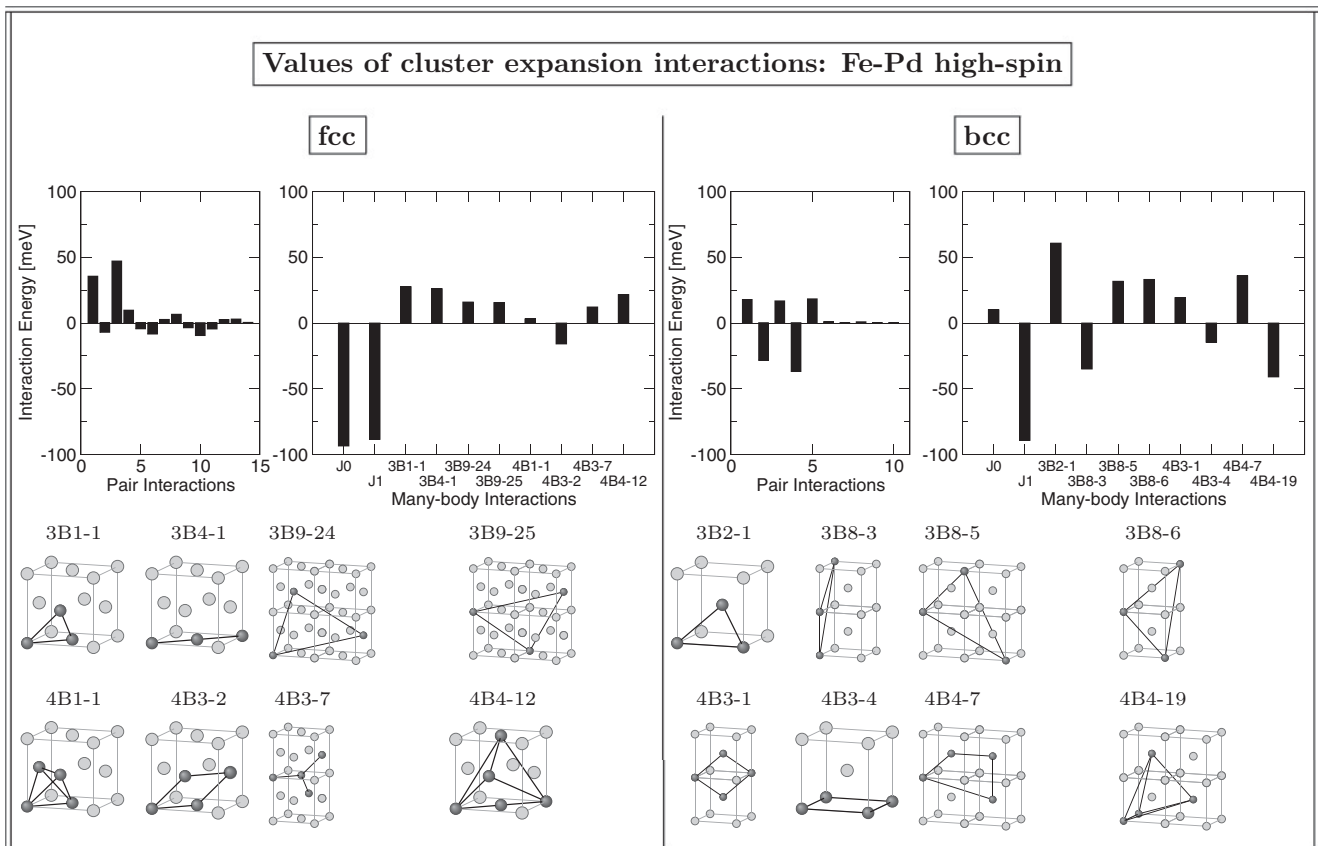


FIG. 6. Values of pair and many-body (MBIT) interaction parameters defining our final fcc and bcc Fe-Pd cluster expansions. The corresponding MBITs clusters are also shown. The MBIT code identifies the corresponding number of vertices and largest separation between those vertices.

fcc cluster expansion, the number of new fcc locally stable predictions declines to zero after nine iterations, requiring a total of 83 input structures. In case of bcc cluster expansion, the required total numbers of iterations and input structures are five and 32, respectively.

From Table I it follows that, had we not used the “outer loop iterations” (see Fig. 4) and instead used just the results of the first iteration, we would have found 13 predicted ground states. However, 7 of the 13 predicted ground states are refuted by DFT and one additional structure is not locally stable in fcc. Even if we had examined the results of the first iteration by DFT and identified the seven incorrect predictions, among the remaining  $13 - 7 - 1 = 5$  ground states [listed under (b1) in Table I] only two ( $\beta 2$  and FePd<sub>5</sub>) are among the final DFT ground states [item (a)=(e7) in Table I] and the other three (DO<sub>23</sub>, FePd<sub>7</sub>, and FePd<sub>14</sub>) are false ground-state predictions, removed by subsequent iterations.

Within our methodology, the “ground-state predictions” are those structures (among all  $\sim 2^{20}$  checked) that are predicted as energetically sufficiently deep and statistically frequent ground states by a number of the best (with highest cross-validation scores) cluster expansions generated at each iteration step.<sup>21</sup> Such statistical procedure allows one to efficiently search for new ground states. However, the ground-state predictions may be different from DFT ground states even at the last iteration step. According to our criteria, such a disagreement is acceptable if it has been tested and is numerically negligible. Namely, in fcc case, two structures (Fe<sub>3</sub>Pd<sub>9</sub> and Fe<sub>2</sub>Pd<sub>13</sub>) from the “DFT convex hull” [item (a)=(e7) in Table I] are not present in the list of correct predictions at iteration step IT=8 [item (b8) in Table I]. This is because the Fe<sub>3</sub>Pd<sub>9</sub> structure is not predicted to be a ground state by any of the considered (twelve) cluster expansions. Nevertheless, its formation energy is predicted by all cluster expansions to be less than 1 meV/atom above the final DFT convex hull. Another structure Fe<sub>2</sub>Pd<sub>13</sub> is predicted to be a ground state by eleven of twelve considered cluster expansions, but in all cases, its depth with respect to the DFT final convex hull is less than 1 meV/atom. Thus, according to our criteria, it is not considered as a correct prediction for a subsequent DFT verification.

In the bcc case, one structure (FePd<sub>8</sub>) from the “DFT convex hull” [item (a)=(e1) in Table II] is not included in the list of correct predictions at iteration step IT = 4 [item (b4) in Table II]. This is because the FePd<sub>8</sub> structure is predicted to be a ground state only by four of the considered (seventeen) cluster expansions (thus according to our criteria it is not considered as a correct prediction for a subsequent DFT verification). Nevertheless, even in those unfavorable thirteen cases its formation energy is predicted to be less than 1 meV/atom above the DFT final convex hull. Note that many bcc structures in the Pd-rich regions decayed into fcc ones, leaving only a small number of candidate structures to do bcc cluster expansion.

The obtained results are consistent with the predictive accuracy of fcc and bcc cluster expansions as estimated by the cross-validation scores (5 and 6.5 meV, respectively, at final iteration steps). The difference between the ground-state predictions and the DFT ground states is not crucial as we keep

and update the DFT convex hull between the iteration steps (see Tables I and II).

Note that both fcc and bcc cases follow exactly the same approach. The smaller number of inputs used for the final bcc CE is mostly due to a higher instability ratio in the bcc case. The resulting accuracies of the bcc and fcc CEs are very similar.

### C. DFT convex hull

The DFT convex hull<sup>57,58</sup> is composed by the structures identified among the  $\sim 100$  structures by DFT during all the outer loop iterations as confirmed ground-state predictions, which we identify as the DFT ground-state structures. These structures are presented in Fig. 7 as well as in Table I [(e7)=(a), fcc case] and in Table II [(e1)=(a), bcc case]. We distinguish four regimes summarized in Table III.

#### 1. Fcc constrained ground states (in the absence of bcc competition)

Fcc Fe and FePd (L<sub>10</sub>) are the ground states only if we neglect the bcc competition. Otherwise, fcc Fe is 151.4 meV/atom less stable than bcc Fe, and FePd L<sub>10</sub> is 25.4 meV/atom less stable than the phase separated mixture of bcc Fe and fcc-FePd<sub>2</sub> ( $\beta 2$ ) at equiatomic composition (dashed line in Fig. 7). This means that at  $T = 0$ , L<sub>10</sub> structure is only a constrained ground state in Fe-Pd and may be observed at low temperatures only if the phase separation of fcc L<sub>10</sub> into the incoherent bcc-Fe + fcc-FePd<sub>2</sub> mixture is kinetically frozen. At higher temperatures, L<sub>10</sub> can be stabilized by the vibrational and spin excitation contributions: indeed, these contributions decrease the free energy of fcc Fe relative to that of bcc Fe, eventually reversing the fcc Fe versus bcc Fe stability; it appears likely that the energy of a general Fe-based fcc alloy would be similarly decreased relative to the bcc Fe. The absence of other fcc-restricted ground states at  $x_{\text{Pd}} < 0.5$  is due to a predicted martensitic fcc  $\rightarrow$  bcc instabilities: all the fcc structures in this composition range that are predicted by the fcc cluster expansion to have low formation enthalpies relax without a barrier to bcc-like configurations. (Nevertheless, they do not produce bcc-restricted ground states upon relaxation, see below.)

#### 2. Absolute fcc ground states (including bcc competition)

Figure 7 reveals the following absolute fcc ground states: FePd<sub>2</sub> ( $\beta 2$ ), Fe<sub>3</sub>Pd<sub>9</sub>, Fe<sub>2</sub>Pd<sub>7</sub>, FePd<sub>5</sub>, Fe<sub>2</sub>Pd<sub>13</sub>, and FePd<sub>8</sub>. These structures are the ground states regardless of whether the bcc competition is considered. In fact, all these structures can be considered derivatives of FePd<sub>2</sub> ( $\beta 2$ ) obtained by substitution of some iron atoms by palladium as required by stoichiometry, and are formed by repeating a three-layer unit with two (100) layers of pure Pd followed by a single (100) mixed Fe-Pd layer. Of all these structures, only FePd<sub>8</sub> has a relatively commonly observed experimental prototype, Pt<sub>8</sub>Ti. Remarkably, the bcc-restricted ground state FePd<sub>2</sub> C11b (discussed in the next subsection) is also crystallographically equivalent (differing only by the value of the  $c/a$  ratio) to fcc FePd<sub>2</sub> ( $\beta 2$ ). Another unexpected finding is that at 75 at.% Pd, it is not the experimentally observed L<sub>12</sub> that is stablest at

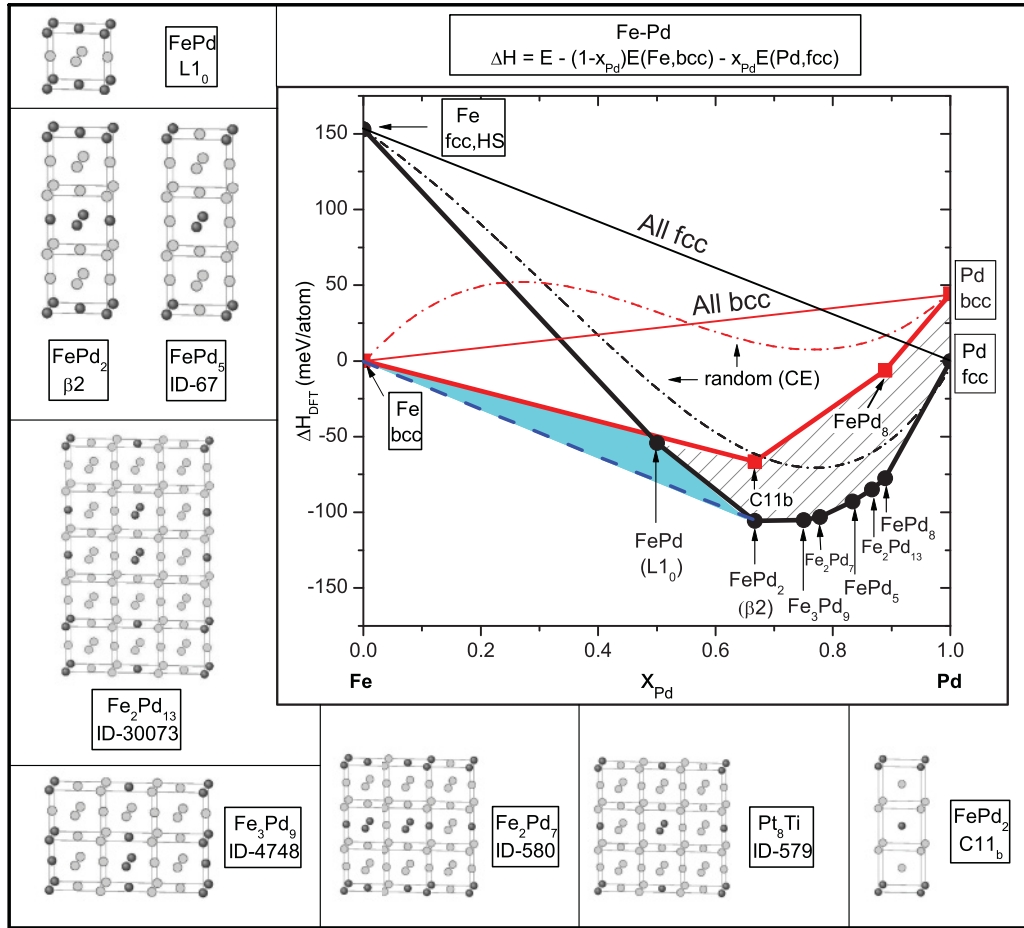


FIG. 7. (Color online) DFT convex hull of fcc (black lines and dots) and bcc (red lines and squares). The values of formation energies are calculated using bcc-Fe and fcc-Pd as reference states:  $\Delta H = E(\sigma) - x_{Fe}E[Fe,bcc] - x_{Pd}E[Pd,fcc]$ . The dashed blue line shows the decomposition into bcc Fe and fcc  $\beta 2$ . The smallest rectangular unit cell (same as the conventional cell for high-symmetry structures) is presented for all the ground states except bcc (124)  $FePd_8$  ordered superlattice (ID-619), for which such a unit cell is too large ( $9 \times 9 \times 9$  bcc cubes); see Supplemental Material<sup>55</sup> for explicit data involving all the ground states. For comparison, we also presented the formation energies of fcc and bcc random alloys [“random (CE)”] obtained by using the final cluster expansions.

$T = 0$ , but one of these  $\beta 2$ -based structures, which can also be described as a superlattice formed by the  $Fe_3Pd_9$  sequence of (430)-oriented layers of pure Fe and Pd. This structure

has a formation energy 4.9 meV/atom lower than  $L1_2$ . Even  $D0_{23}$  structure is lower in energy than  $L1_2$  by 4.0 meV/atom. We confirmed that spin-orbit coupling does not change this

TABLE III. Fe-Pd DFT ground states and the structures observed experimentally<sup>5</sup> (at 600 K). “fcc (bcc) constrained” means that the corresponding fcc (bcc) structures are the ground states *only* if the fcc (bcc) structures are taking into account. “fcc (bcc) absolute” means that the corresponding fcc (bcc) structures are ground states if both fcc and bcc structures are taking into account. For the DFT energies, please refer to the Tables VI–VIII in the appendixes.

$x_{Pd}$	fcc constrained	fcc absolute	bcc constrained	bcc absolute	Exp. 600 K
0.00	Fe,fcc			Fe,bcc	Fe,bcc
0.50	$L1_0$				$L1_0$
2/3		$\beta 2$	$C11_b$		$L1_2$
0.75		$Fe_3Pd_9$			$L1_2$
0.7(7)		$Fe_2Pd_7$			$L1_2$
0.8(3)		$FePd_5$			$L1_2$
0.8(6)		$Fe_2Pd_{13}$			Disorder
0.8(8)		$FePd_5$	$FePd_8$		Disorder
1.00		$Pd,fcc$	$Pd,bcc$		$Pd,fcc$

hierarchy leaving  $\text{FePd}_3$  ( $L1_2$ ) still 3.0 meV/atom higher in energy than  $\text{Fe}_2\text{Pd}_6$  ( $\text{DO}_{23}$ ). We also checked (see EPAPS<sup>55</sup>) that the use of different pseudopotentials does not change the energy hierarchy of  $L1_2$ ,  $\text{DO}_{23}$ , and  $\text{Fe}_3\text{Pd}_9$  (ID-4748).

### 3. Bcc ground states (in the absence of fcc competition)

$\text{FePd}_2$  C11b and (124) superlattice bcc- $\text{FePd}_8$  are the ground states only if we neglect fcc competition at  $T = 0$ . These structures are hardly of any practical interest, since raising the temperature should only further destabilize the bcc-based structures (by analogy with pure iron). Notably, there are no bcc ground states in the Fe-rich part of the diagram. Figure 7 shows the energies of fcc and bcc random alloys obtained from the cluster expansions. The random alloy approximates the expected behavior of the Fe-Pd system at high temperatures (cf. Sec. V A). We see that for the bcc alloy, this energy is positive and has a negative second derivative in the Fe-rich region, indicating that the existence of such alloy is thermodynamically unstable and would undergo a spinodal decomposition. Together with the above-mentioned martensitic instability of the fcc-based alloy at this composition, this indicates that it should not be possible to obtain *any* form of Fe-rich Fe-Pd alloy, in agreement with experiment.

### 4. Absolute bcc ground states (including fcc competition)

Bcc Fe is the only bcc structure that is the ground state regardless of whether fcc competition is considered.

### D. Final cluster expansions

In Fig. 8, we present the formation energies of all the  $\sim 2^{20}$  structures (enumerated with the method of Ref. 56) as predicted by the final cluster expansions in fcc and bcc Fe-Pd. The fcc ground-state structures may be classified as

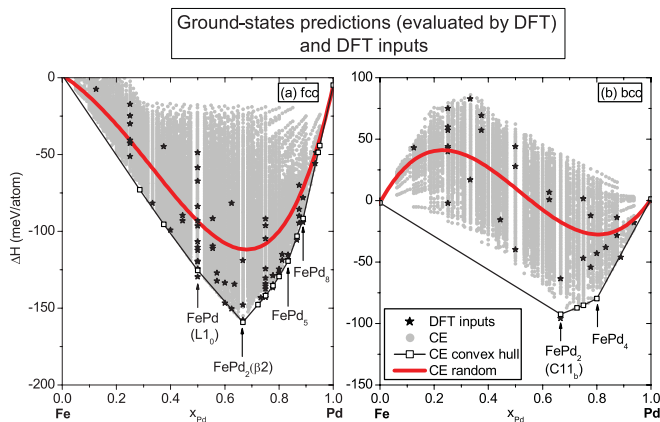


FIG. 8. (Color online) DFT formation energies of all input structures as well as the formation energies of all possible structures with less or equal 20 (fcc) and 16 (bcc) atoms per unit cell generated by the corresponding final cluster expansions (CE) in (a) fcc and (b) bcc Fe-Pd. Based on the cluster expansions the corresponding convex hulls are built. The formation energies of random alloys are also shown. Note that in contrast to Fig. 7, both reference states (pure iron and palladium) for calculation of  $\Delta H$  are chosen to be (a) fcc and (b) bcc. Only the sufficiently deep ground states (deeper than 1 meV/atom) are labeled.

following. Four structures  $\text{FePd}$  ( $L1_0$ ),  $\text{FePd}_2$  ( $\beta 2$ ),  $\text{FePd}_5$ , and  $\text{FePd}_8$  found on the DFT convex hull [listings (a) = (e7) in Table I] are deep ground states. Those structures are labeled in Fig. 8(a). Two structures ( $\text{Fe}_2\text{Pd}_7$  and  $\text{Fe}_2\text{Pd}_{13}$ ) found on the DFT convex hull are shallower than 1 meV/atom ground states. One structure ( $\text{Fe}_3\text{Pd}_9$ ) found on the DFT convex hull is not predicted as a ground state by the cluster expansion, but its formation energy is less than 1 meV/atom higher than that of the predicted ground state at this composition. Seven additional structures (not present on the DFT convex hull) are predicted to be shallower than 1 meV/atom ground states.

The bcc ground-state structures may be classified as following. One structure  $\text{FePd}_2$  (C11b) found on the DFT convex hull [listings (a) = (e1) in Table II] is a deep ground state. This is one of the two structures labeled in Fig. 8(b). The other structure  $\text{FePd}_8$  found on the DFT convex hull is not a ground state in cluster expansion, but its formation energy is less than 1 meV/atom higher than that of the predicted ground state at this composition.

One structure  $\text{FePd}_4$  is predicted to be a deep ground state. However, it is not present on the DFT convex hull because it is found to be bcc locally unstable [see listings (d2)–(d5) in Table II]. This structure is also labeled in Fig. 8(b). Two additional structures (not present on the DFT convex hull) are predicted as ground states shallower than 1 meV/atom.

All these minor conflicts between the DFT and the cluster expansion arise due to the finite (albeit small) cross-validation score of the chosen final cluster expansions, which becomes important due to the adaptive character<sup>52</sup> of all the obtained global ground states except  $\text{FePd}_2$  ( $\beta 2$ ).

### E. Comparison with previous Fe-Pd cluster expansions

In a series of papers Mohri *et al.*<sup>31</sup> derived a number of fcc-HS Fe-Pd cluster expansions based on different sets of first-principles formation energies. The largest set consists of  $L1_0$ ,  $L1_1$ ,  $L1_2$ , and  $\text{DO}_{23}$ . The largest cluster expansion includes two-, three-, and four-body nearest neighbors, pair next nearest neighbor as well as irregular triangle and irregular

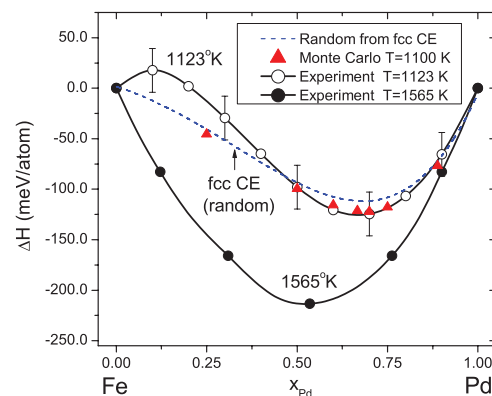


FIG. 9. (Color online) Formation enthalpies  $\Delta H$  (with fcc-Fe and fcc-Pd as reference states) calculated by the use of fcc-HS cluster expansion in case of completely random phase and by Monte Carlo simulation at  $T = 1100$  K (see Fig. 10) and obtained experimentally for disordered paramagnetic state at  $T = 1125$  K (see Ref. 48) and  $1565$  K (see Ref. 49).

tetrahedron cluster interactions. The formation energies of all the ordered structures considered by Mohri *et al.* are calculated as functions of volume neglecting cell-internal and cell-shape relaxations. At any given volume, the cluster interactions are calculated using the formation energies of all considered structures at the same volume, thus making the cluster interactions to be functions of volume. At any value of composition and temperature, the functional of free energy

(containing those cluster interactions and considered within the cluster-variation method) was minimized with respect to volume. Using such a functional of free energy, the transition temperatures for L1<sub>0</sub>-disorder transition are obtained to be 1080, 1505, and 1760 K for three considered sets of cluster interactions, respectively. The phase transition temperature was considerably decreased toward the experimental value by the use of Debye-Grüneisen model for vibrational free

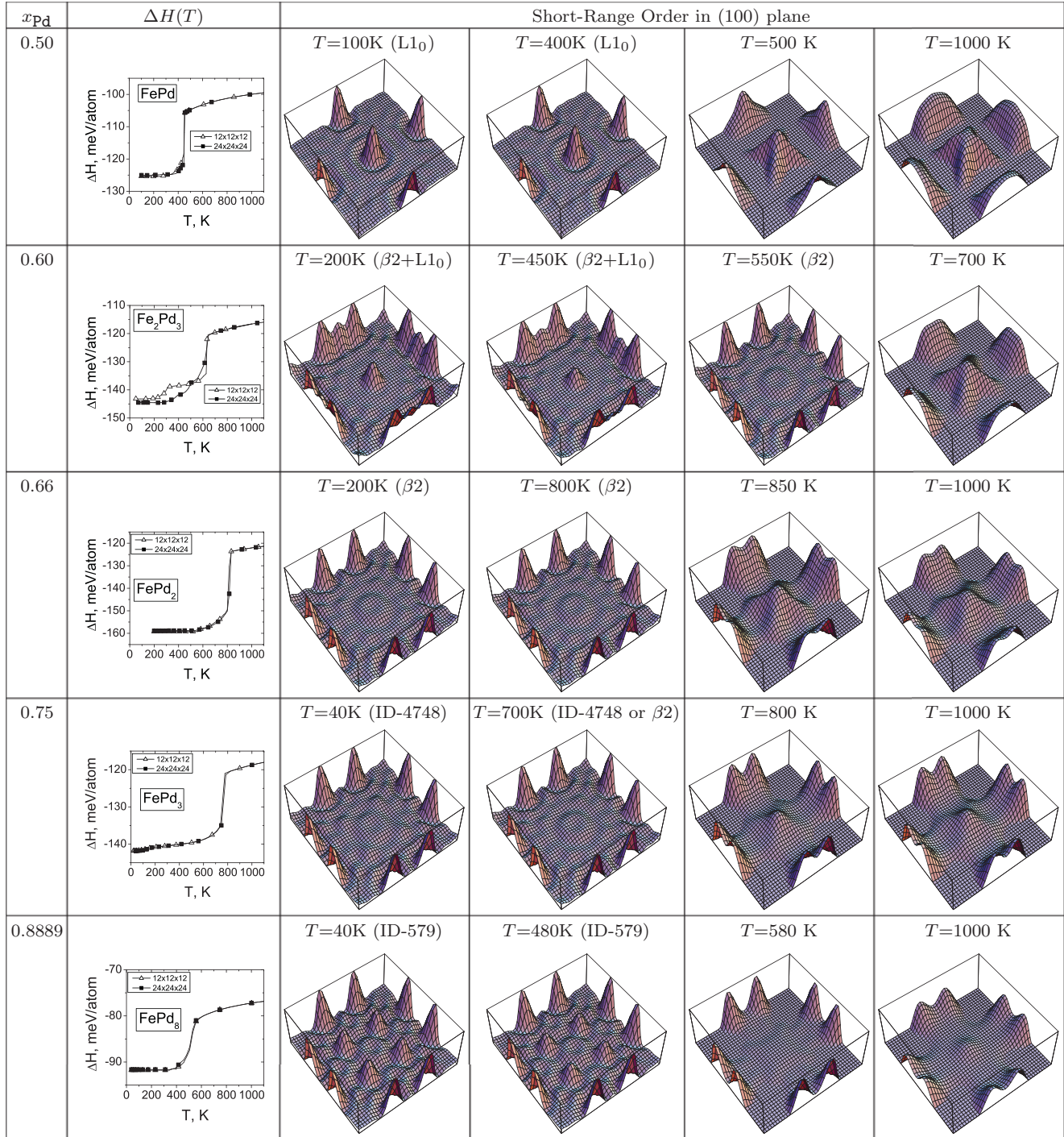


FIG. 10. (Color online) Fcc Monte Carlo simulation of formation energy  $\Delta H$  and short-range order in (100) plane as function of temperature and composition. The corners of each square correspond to  $\Gamma$  points, whereas the center of the square as well as the center of each edge correspond to  $X = \{1,0,0\}$  points. Note that different simulation temperatures are selected for different compositions within the same figure column.

energy. It was argued that such vibrational contribution partly describes the local relaxations of atoms.

The detailed comparison and discussion of formation energies obtained in Ref. 31 and in the present study is done in Appendix A. The only common feature of the cluster interactions obtained in the present paper and in Ref. 31 is the large positive value of the nearest neighbor interaction. We attribute the difference in cluster expansions to the much larger structure pull (83 structures built iteratively) used in the present study.

## V. PHASE STABILITY AT FINITE TEMPERATURES

The obtained cluster expansions are targeted to correctly reproduce the corresponding ground states. Nevertheless, the structures far from convex hulls are also included into the cluster expansion fits. So we expect that the calculated cluster expansions give a reasonable error in the description of high-energy structures as well, thus allowing one to evaluate the configurational high-temperature properties. Such theoretical predictions may be directly compared with experimental data, which are usually obtained at finite (usually high enough) temperatures. In this section, such high-temperature properties as the atomic short-range order and the heat of formation of the disordered phase are calculated on the basis of the cluster expansion for a wide compositional range.

### A. Mixing enthalpies

In Fig. 9, we present a comparison of the mixing enthalpies calculated from our fcc high-spin cluster expansion for random (completely disordered) alloy, for disordered alloy at  $T = 1100$  K (by Monte Carlo simulations, see Fig. 10) and obtained experimentally<sup>48,49</sup> for disordered paramagnetic state at different temperatures and compositions. Figure 9 demonstrates that the random alloy gives a good approximation for the Fe-Pd formation energy at sufficiently high temperatures. The high-spin cluster expansion does not include the phonon contribution that may be responsible for part of the difference between the experimental (at lowest available temperature) and theoretical data. The possible importance of the phonon contribution is manifested by a large difference between the two experimental curves corresponding to different temperatures (1123 and 1565 K).

The other possible reason of the difference between experimental (1123 K) and theoretical curve is that the used cluster expansion is based on ferromagnetic high-spin states whereas the measured states are *paramagnetic*. Nevertheless, the calculated results are noticeably within the experimental error of  $T = 1123$  K measurements.

### B. Short-range order and transition temperatures

We can now use the final fcc-HS cluster expansion to perform canonical Monte Carlo simulations<sup>24</sup> of the fcc alloy, allowing us to study the temperature ( $T$ ) dependence of the formation energies  $\Delta H$  and short-range order in (100) fcc reciprocal plane for a number of compositions (see Fig. 10). At each temperature, we use 1000 and 100 flips/site to achieve equilibrium and average the energy, respectively. In order to reduce the risk of poor convergence at low temperatures, we

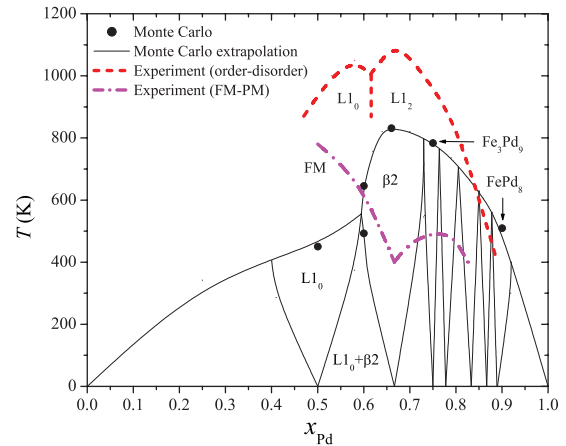


FIG. 11. (Color online) Fe-Pd fcc phase diagram extrapolated from Monte Carlo simulation, compared to that measured experimentally<sup>5,8,9</sup> (FM is ferromagnetic, PM is paramagnetic). The solid lines sketch possible phase boundaries, including those of hypothetical phases corresponding to the  $T = 0$  ground state structures. (This sketch does not reflect the possibility of peritectoid and most other phase-segregating transitions, even when strictly speaking such transitions are required thermodynamically.)

use progressively smaller temperature steps with temperature decrease. The sample sizes used for Monte Carlo simulation are indicated in the  $\Delta H(T)$  plots. The purpose of using the large sample sizes is to avoid the finite-size effects on order-disorder transition. The abrupt change in  $\Delta H(T)$  corresponds to a phase transition. From Fig. 10 we obtain the following results, which are extrapolated into a tentative fcc-restricted phase-composition phase diagram shown in Fig. 11.

At compositions  $x_{Pd} = 0.50$ , the peaks at  $\mathbf{k} = \{1,0,0\}$  points are obtained, reflecting the expected  $L1_0$  ordering below the order-disorder transition temperature  $T_{ord} = 450$  K. Similarly, the ordering evidenced at  $x_{Pd} = 0.66$  by the peaks at  $\mathbf{k} = \{1/3,0,0\}$  is  $\beta_2$ , predicted by the cluster expansion at that composition, with  $T_{ord} = 832$  K. At an intermediate composition  $x_{Pd} = 0.60$ , the order-disorder phase transition to  $\beta_2$  structure is observed at  $T_{ord} = 645$  K, evidenced by the well defined  $\mathbf{k} = \{1/3,0,0\}$  peaks below  $T_{ord}$ . However, below 505 K, additional  $\mathbf{k} = \{1,0,0\}$  peaks appear, which

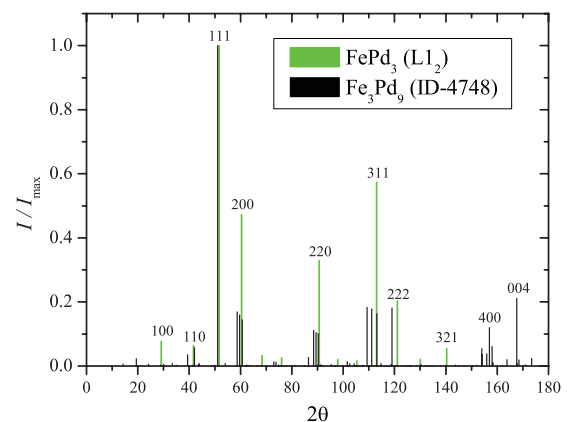


FIG. 12. (Color online) Simulated diffractograms for the *ab initio* fully relaxed  $FePd_3$  ( $L1_2$ ) and  $Fe_3Pd_9$  (ID-4748) structures.

we interpret as a possible indication of a phase separation into  $L1_0$  and  $\beta 2$  structures below 505 K.

At compositions  $x_{Pd} = 0.75$  and  $x_{Pd} = 0.89$ , the phase transitions into  $Fe_3Pd_9$  (ID-4748) and  $FePd_8$  (ID-579) structures are observed at 784 and 510 K, respectively. In both cases the dominant peak at  $(1/3,0,0)$  reflects the  $\beta 2$ -like nature of both structures. At  $x_{Pd} = 0.75$ , the diffuse peaks at  $T > T_{ord}$  merge somewhat compared to the perfect  $(1/3,0,0)$  positions at  $T < T_{ord}$ , and may look more like split (100)

TABLE IV. Theoretical and experimental data for magnetic moment  $\mu$ , lattice parameter  $a$ , and energy  $E$  (with respect to the energy of bcc Fe) of iron in bcc, fcc-LS, and fcc-HS configurations as well as of palladium in fcc configuration.

SYSTEM	METHOD	$\mu$ ( $\mu_B$ )	$a$ ( $\text{\AA}$ )	$E$ (meV/atom)
Fe, bcc	PAW-GGA <sup>a</sup>	2.21	2.84	
	FLAPW-GGA <sup>b</sup>		2.83	
	FLAPW-GGA <sup>c</sup>	2.17	2.84	
	FLAPW-GGA <sup>d</sup>		2.84	0
	FLAPW-GGA <sup>e</sup>	2.17	2.83	
	Exp. <sup>f</sup>	2.22		
	Exp.(298 K) <sup>g</sup>		2.87	
Fe, fcc LS	PAW-GGA <sup>a</sup>	0.70	3.47	139.4
	FLAPW-GGA <sup>c</sup>	1.02	3.49	126.6
	FLAPW-GGA <sup>d</sup>	1.05	3.49	136.1
	FLAPW-GGA <sup>h</sup>	1.04	3.54	138.9
	FLAPW-GGA <sup>e</sup>	1.34	3.48	129.0
	Exp. <sup>i</sup>	0.72-0.74		
Fe, fcc HS	PAW-GGA <sup>a</sup>	2.59	3.64	151.4
	FLAPW-GGA <sup>c</sup>	2.57	3.64	153.3
	FLAPW-GGA <sup>h</sup>	2.56	3.64	147.9
	Exp.(1193 K) <sup>g</sup>		3.65	
Pd, fcc	PAW-GGA <sup>a</sup>	0.35	3.96	
	FLAPW-GGA <sup>b</sup>		3.94	
	FLAPW-GGA <sup>d</sup>	0.18	3.93	
	Exp.(293 K) <sup>g</sup>		3.89	

<sup>a</sup>Present PAW calculations using the VASP code<sup>27</sup> and GGA of Perdew and Wang<sup>25</sup> with parametrization of Vosko, Wilk, and Nusair<sup>26</sup> [with 240 (bcc) and 408 (fcc) irreducible  $k$  points for integration and 400 eV energy cutoff for the wave function].

<sup>b</sup>Calculations of Asato *et al.*, Ref. 28, using the Jülich FLAPW code and GGA of Perdew and Wang<sup>25</sup> with parametrization of Moruzzi, Janak, and Williams, Ref. 29.

<sup>c</sup>FLAPW calculations of Herper *et al.*, Ref. 30, using the WIEN95 code and GGA of Perdew and Wang<sup>25</sup> (with 145 irreducible  $k$  points for integration and 320 eV energy cutoff for the wave function).

<sup>d</sup>FLAPW calculations of Mohri *et al.*, Ref. 31, using GGA of Perdew and Wang<sup>25</sup> [with 85 (fcc) and 84 ( $L1_0$ ,  $L1_2$ ) irreducible  $k$  points for integration and 272 eV energy cutoff for the wave function].

<sup>e</sup>FLAPW calculations of Mishin *et al.*, Ref. 32, using GGA of Perdew and Wang<sup>25</sup> [with 285 (bcc) and 489 (fcc) irreducible  $k$  points for integration and 450 eV energy cutoff for the wave function].

<sup>f</sup>Reference 33.

<sup>g</sup>Pearsons Handbook, Ref. 34.

<sup>h</sup>FLAPW calculations of Timoshevskii *et al.*, Ref. 35, using the WIEN97 code and GGA of Perdew-Burke-Ernzerhof<sup>36</sup> (with 84 irreducible  $k$  points for integration and 411 eV energy cutoff for the wave function).

<sup>i</sup>Abrahams *et al.*,  $T = 4$  K, Ref. 37.

peaks. Since  $L1_2$  structure at this composition would be also characterized by (100) peaks, it might appear that at  $x_{Pd} \geq 2/3$ , the configurational entropy has a tendency to transform  $\beta 2$  to  $L1_2$ , but this tendency is not strong enough for the  $\beta 2$  to  $L1_2$  order-order transition to occur. However, such a tendency would be highly speculative, since, generally, the diffuse short-range order (SRO) peaks do not necessarily appear at the same positions as the long-range order (LRO) ordering vectors.

TABLE V. Theoretical and experimental data for  $L1_2$  and  $L1_0$  structures on magnetic moments (in  $\mu_B$ ) of unit cell ( $\mu_{u.c.}$ ), iron ( $\mu_{Fe}$ ) and palladium ( $\mu_{Pd}$ ) atoms as well as lattice parameter  $a$ , tetragonality ( $c/a$ ), and heats of formation (in meV/at.) with respect to fcc-HS iron and bcc iron ( $\Delta H_1$  and  $\Delta H_2$ , respectively).

METHOD	$\mu_{u.c.}$	$\mu_{Fe}$	$\mu_{Pd}$	$a$ ( $\text{\AA}$ )	$c/a$	$\Delta H_1^a$	$\Delta H_2^a$
<b>Fe<sub>3</sub>Pd, L1<sub>2</sub></b>							
PAW-GGA <sup>b</sup>	8.43	2.73	0.36	3.73		-42.7	70.9
FLAPW-GGA <sup>c</sup>	8.64	2.76	0.36	3.74			108.8
PAW-GGA <sup>d</sup>				3.76			
Exp.(623 K) <sup>e</sup>				3.82			
Exp.(1123 K) <sup>f</sup>						-12.8	( $\pm 21.7$ )
<b>FePd, L1<sub>0</sub></b>							
PAW-GGA <sup>b</sup>	3.30	2.96	0.38	3.85	0.98	-129.7	-54.0
FLAPW-GGA <sup>c</sup>	3.30	2.94	0.35	3.81	0.98		-46.3
FP-LAPW <sup>g</sup>	3.43						
Exp.(700 K) <sup>e</sup>				3.86	0.96		
Exp.(1123 K) <sup>f</sup>						-97.9	( $\pm 21.7$ )
<b>FePd<sub>3</sub>, L1<sub>2</sub></b>							
PAW-GGA <sup>b</sup>	4.32	3.27	0.36	3.90		-138.5	-100.6
FLAPW-GGA <sup>c</sup>	4.32	3.32	0.34	3.90			-54.4
Exp.(700 K) <sup>e</sup>				3.86			
Exp.(1123 K) <sup>f</sup>						-118.5	( $\pm 21.7$ )
Exp. <sup>h</sup>	4.59						
	( $\pm 0.03$ )						
Exp. <sup>i</sup>	4.36	3.10	0.42				

<sup>a</sup> $\Delta H_1 = E(\sigma) - x_{Fe}E[Fe, fcc-HS] - x_{Pd}E[Pd, fcc]$ ,  $\Delta H_2 = E(\sigma) - x_{Fe}E[Fe, bcc] - x_{Pd}E[Pd, fcc]$ .

<sup>b</sup>Present PAW calculations using the VASP code<sup>27</sup> and GGA approximation of Perdew and Wang<sup>25</sup> with parametrization of Vosko, Wilk, and Nusair (see Ref. 26) [with 120 ( $L1_2$ ) and 576 ( $L1_0$ ) irreducible  $k$  points for integration and 400 eV energy cutoff].

<sup>c</sup>FLAPW calculations of T. Mohri *et al.*, Ref. 31, using GGA approximation of Perdew and Wang<sup>25</sup> [with 85 (fcc) and 84 ( $L1_0$ ,  $L1_2$ ) irreducible  $k$  points for integration and 272 eV energy cutoff for the wave function].

<sup>d</sup>PAW potential calculations of R. R. Duplessis *et al.*, Ref. 38, using the VASP code<sup>27</sup> and GGA approximation of Perdew and Wang<sup>25</sup> with parametrization of Vosko, Wilk, and Nusair, Ref. 26.

<sup>e</sup>Pearson's Handbook, Ref. 34.

<sup>f</sup>C. B. Alcock *et al.*, R. Hultgren *et al.*, and O. Kubaschewski *et al.*,  $T = 1123$  K (disordered, paramagnetic state), Ref. 39.

<sup>g</sup>FP-LAPW calculations of M. Elzain *et al.*, Ref. 40, using the WIEN2K code.

<sup>h</sup>M. H. P. Corrêa *et al.*, Ref. 41.

<sup>i</sup>J. W. Cable *et al.*, Ref. 42.

TABLE VI. Fcc formation energies  $\Delta H = E(\sigma) - x_{\text{Fe}}E[\text{Fe, fcc-HS}] - x_{\text{Pd}}E[\text{Pd, fcc}]$  (meV/atom) of the DFT input structures at  $x_{\text{Pd}} < 0.75$  used for the Fe-Pd fcc cluster expansion. “ID” corresponds to the index in our structural database ( $\Pi$  file), “PR” means prototype, “Superlattice notation” describes orientation (hkl) and stoichiometry of layers when the structure is a superlattice (“None” means nonsuperlattice), “IT” denotes the outer loop iteration number when the structure is first predicted to be a possible ground state, symbols “\*” in IT column denote the final DFT fcc ground states, and A1 means fcc HS.

ID	Stoich.	$x_{\text{Pd}}$	PR	Superlattice notation	$\Delta H$ DFT	$\Delta H$ CE	IT
0	Fe	0.000	A1		0.0	1.6	0
371	Fe <sub>7</sub> Pd	0.125	D1	None	-7.5	-5.5	0
211	Fe <sub>6</sub> Pd <sub>2</sub>	0.250		(115)A <sub>6</sub> B <sub>2</sub>	-51.2	-58.4	8
15	Fe <sub>3</sub> Pd		L1 <sub>2</sub>	None	-42.7	-48.1	0
282	Fe <sub>6</sub> Pd <sub>2</sub>		DO <sub>23</sub>	(401)A <sub>5</sub> BAB	-40.6	-36.5	0
11	Fe <sub>3</sub> Pd		W1	(311)A <sub>3</sub> B	-30.0	-27.0	0
10	Fe <sub>3</sub> Pd		L1 <sub>3</sub>	None	-24.8	-24.7	0
4	Fe <sub>2</sub> Pd	0.333	$\beta$ 1	(001)A <sub>2</sub> B	-81.8	-83.0	0
91210	Fe <sub>10</sub> Pd <sub>6</sub>	0.375		None	-85.3	82.6	3
372	Fe <sub>5</sub> Pd <sub>3</sub>		D3	None	-44.9	-44.5	0
23	Fe <sub>3</sub> Pd <sub>2</sub>	0.400		(001)A <sub>2</sub> BAB	-99.1	-98.9	5
588	Fe <sub>5</sub> Pd <sub>4</sub>	0.444		None	-93.0	-96.5	1
585	Fe <sub>5</sub> Pd <sub>4</sub>			None	-89.6	-88.9	1
1	FePd	0.500	L1 <sub>0</sub>	(001)AB	-129.6	-125.4	0*
12	Fe <sub>2</sub> Pd <sub>2</sub>		W2	(311)A <sub>2</sub> B <sub>2</sub>	-124.3	-122.0	0
9	Fe <sub>2</sub> Pd <sub>2</sub>		Z2	(001)A <sub>2</sub> B <sub>2</sub>	-119.8	-119.5	0
7	Fe <sub>2</sub> Pd <sub>2</sub>		Y2	(011)A <sub>2</sub> B <sub>2</sub>	-119.4	-116.2	0
289	Fe <sub>4</sub> Pd <sub>4</sub>			(014)A <sub>4</sub> B <sub>4</sub>	-112.4	-113.4	1
303	Fe <sub>4</sub> Pd <sub>4</sub>			(013)A <sub>4</sub> B <sub>4</sub>	-110.5	-114.1	4
91218	Fe <sub>8</sub> Pd <sub>8</sub>			None	-107.1	-111.8	3
3258	Fe <sub>6</sub> Pd <sub>6</sub>			None	-106.7	-111.2	7
286	Fe <sub>4</sub> Pd <sub>4</sub>			(014)A <sub>3</sub> B <sub>2</sub> AB <sub>2</sub>	-96.4	-98.7	4
307	Fe <sub>4</sub> Pd <sub>4</sub>			(013)A <sub>3</sub> B <sub>2</sub> AB <sub>2</sub>	-93.2	-93.2	4
17	Fe <sub>2</sub> Pd <sub>2</sub>		CH	(201)A <sub>2</sub> B <sub>2</sub>	-83.7	-82.5	0
2	FePd		L1 <sub>1</sub>	(111)AB	-58.6	-60.8	0
373	Fe <sub>4</sub> Pd <sub>4</sub>		D4	None	-48.8	-47.2	0
627	Fe <sub>4</sub> Pd <sub>5</sub>	0.556		None	-111.1	-103.6	2
585	Fe <sub>4</sub> Pd <sub>5</sub>			None	-109.6	-105.0	1
588	Fe <sub>4</sub> Pd <sub>5</sub>			None	-91.8	-97.2	2
91235	Fe <sub>7</sub> Pd <sub>9</sub>	0.563		None	-120.4	-116.9	3
112	Fe <sub>3</sub> Pd <sub>4</sub>	0.571		(112)AB <sub>2</sub> ABAB	-132.3	-132.0	4
129	Fe <sub>3</sub> Pd <sub>4</sub>			(012)ABAB <sub>2</sub> AB	-127.1	-126.2	4
23	Fe <sub>2</sub> Pd <sub>3</sub>	0.600		(001)ABAB <sub>2</sub>	-146.7	-144.8	1
20	Fe <sub>2</sub> Pd <sub>3</sub>			(011)A <sub>2</sub> B <sub>3</sub>	-133.6	-136.0	1
160	Fe <sub>3</sub> Pd <sub>5</sub>	0.625		(100)ABAB <sub>2</sub> AB <sub>2</sub>	-150.4	-150.2	5
372	Fe <sub>3</sub> Pd <sub>5</sub>		D5	None	-81.6	-83.5	0
1852	Fe <sub>4</sub> Pd <sub>7</sub>	0.636		(013)AB(AB <sub>2</sub> ) <sub>3</sub>	-134.4	-134.8	4
4	FePd <sub>2</sub>	0.667	$\beta$ 2	(001)AB <sub>2</sub>	-157.7	-159.2	0*
3	FePd <sub>2</sub>		$\gamma$ 2	(011)AB <sub>2</sub>	-148.0	-155.0	0
5	FePd <sub>2</sub>		$\alpha$ 2	(111)AB <sub>2</sub>	-118.9	-117.1	0
16161	Fe <sub>4</sub> Pd <sub>10</sub>	0.714		(014)A <sub>2</sub> B <sub>2</sub> AB <sub>6</sub> AB <sub>2</sub>	-120.2	-117.2	3
36312	Fe <sub>4</sub> Pd <sub>11</sub>	0.733		(653)(AB <sub>2</sub> ) <sub>3</sub> AB <sub>5</sub>	-143.2	-143.4	5

### C. Phase identity: theory versus experiment

All the low-temperature phases obtained via the simulated annealing in these Monte Carlo studies are in agreement with our fcc DFT ground states at the corresponding compositions. Such a result must be expected due to the use of the fcc cluster expansion.

At  $x_{\text{Pd}} = 0.50$ , the simulated L1<sub>0</sub> type of ordering and (100) peak above the phase transition both are in qualitative accordance with corresponding experimental data on the order-

disorder transition<sup>5</sup> and diffuse scattering from substitutionally disordered monocrystal.<sup>51</sup> However, the obtained transition temperature 450 K is considerably lower than the experimental  $\sim 970$  K. A similar underestimated transition temperature was also found by the Monte Carlo simulation using the interaction parameters obtained from the experimental data on the diffuse scattering in Ref. 50.

Because our simulation uses only the fcc cluster expansion, the bcc phase is absent in Fig. 11. However, the experimental

TABLE VII. Same as Table VI but for  $x_{\text{Pd}} \geq 0.75$ .

ID	Stoich.	$x_{\text{Pd}}$	PR	Superlattice notation	$\Delta H$ DFT	$\Delta H$ CE	IT
4748	Fe <sub>3</sub> Pd <sub>9</sub>	0.750		(034)(AB <sub>2</sub> ) <sub>2</sub> AB <sub>5</sub>	-142.9	-141.1	7*
282	Fe <sub>2</sub> Pd <sub>6</sub>		DO <sub>23</sub>	(401)ABAB <sub>5</sub>	-141.4	-138.7	0
15	FePd <sub>3</sub>		L1 <sub>2</sub>	None	-137.5	-138.6	0
16	FePd <sub>3</sub>		DO <sub>22</sub>	(201)AB <sub>3</sub>	-135.6	-140.1	0
300	Fe <sub>2</sub> Pd <sub>6</sub>			(013)AB <sub>5</sub> AB	-134.1	-133.9	4
211	Fe <sub>2</sub> Pd <sub>6</sub>			(115)A <sub>2</sub> B <sub>6</sub>	-132.6	-129.9	3
342	Fe <sub>2</sub> Pd <sub>6</sub>			None	-131.5	-130.4	3
8	FePd <sub>3</sub>		Z3	(001)AB <sub>3</sub>	-130.4	-126.2	0
6	FePd <sub>3</sub>		Y3	(011)AB <sub>3</sub>	-124.3	-127.3	0
11	FePd <sub>3</sub>		W3	(311)AB <sub>3</sub>	-104.9	-104.9	0
63521	Fe <sub>4</sub> Pd <sub>12</sub>			None	-101.9	-105.7	3
13	FePd <sub>3</sub>		V3	(111)AB <sub>3</sub>	-96.3	-99.4	0
10	FePd <sub>3</sub>		L1 <sub>3</sub>	None	-91.8	-92.3	0
580	Fe <sub>2</sub> Pd <sub>7</sub>	0.778		None	-136.6	-135.5	2*
583	Fe <sub>2</sub> Pd <sub>7</sub>			None	-134.7	-123.8	2
541	Fe <sub>2</sub> Pd <sub>7</sub>			(013)AB <sub>2</sub> AB <sub>5</sub>	-128.8	-132.5	4
30123	Fe <sub>3</sub> Pd <sub>12</sub>	0.800		(035)AB <sub>2</sub> (AB <sub>5</sub> ) <sub>2</sub>	-128.5	-129.5	2
1092	Fe <sub>2</sub> Pd <sub>8</sub>			(014)ABAB <sub>7</sub>	-127.3	-124.0	2
28042	Fe <sub>3</sub> Pd <sub>12</sub>			(013)AB <sub>2</sub> (AB <sub>5</sub> ) <sub>2</sub>	-124.6	-127.6	6
1133	Fe <sub>2</sub> Pd <sub>8</sub>			(013)A <sub>2</sub> B <sub>8</sub>	-122.2	-115.9	3
30	FePd <sub>4</sub>			(201)AB <sub>4</sub>	-112.8	-115.8	3
64323	Fe <sub>3</sub> Pd <sub>13</sub>	0.813		(014)ABAB <sub>5</sub> AB <sub>7</sub>	-118.7	-117.2	1
63086	Fe <sub>3</sub> Pd <sub>13</sub>			None	-115.0	-120.1	7
67	FePd <sub>5</sub>	0.833		(301)AB <sub>5</sub>	-118.4	-119.4	1*
6068	Fe <sub>2</sub> Pd <sub>10</sub>			None	-115.2	-114.4	8
4830	Fe <sub>2</sub> Pd <sub>10</sub>			(023)AB <sub>2</sub> AB <sub>8</sub>	-108.0	-106.2	3
7900	Fe <sub>2</sub> Pd <sub>11</sub>	0.846		(013)AB <sub>2</sub> AB <sub>9</sub>	-103.5	-99.4	3
30073	Fe <sub>2</sub> Pd <sub>13</sub>	0.867		(503)AB <sub>5</sub> AB <sub>8</sub>	-105.7	-103.2	2*
279	FePd <sub>7</sub>	0.875		(014)AB <sub>7</sub>	-94.5	-90.7	1
91276	Fe <sub>2</sub> Pd <sub>14</sub>			None	-91.3	-90.4	3
269	FePd <sub>7</sub>			None	-90.0	-93.6	7
290	FePd <sub>7</sub>			None	-85.6	-88.0	1
371	FePd <sub>7</sub>		D <sub>7</sub>	None	-70.0	-69.5	0
579	FePd <sub>8</sub>	0.889	Pt <sub>8</sub> Ti	None	-94.2	-91.8	2*
502	FePd <sub>8</sub>			None	-78.0	-77.1	2
1132	FePd <sub>9</sub>	0.900		(013)AB <sub>9</sub>	-79.2	-80.3	3
15787	FePd <sub>13</sub>	0.929		(014)AB <sub>13</sub>	-58.5	-59.0	3
28503	FePd <sub>14</sub>	0.933		(014)AB <sub>14</sub>	-55.8	-55.4	1
91145	FePd <sub>15</sub>	0.938		None	-48.9	-50.5	8
0	Pd	1.000	A1		0.0	-4.8	0

observation of a bcc  $\rightarrow$  fcc transition in iron suggests that the phonon and/or magnetic entropy contributions raise the free energy of bcc Fe with respect to fcc Fe. If the same tendency keeps for Fe-rich compounds, one would expect that L1<sub>0</sub> becomes stable at higher  $T$ , and the bcc-Fe+FePd<sub>2</sub>( $\beta$ 2) two-phase field predicted here is replaced by bcc-Fe+FePd(L1<sub>0</sub>), as indicated in the experimental phase diagram. The comparatively low L1<sub>0</sub>/disorder transition temperature obtained by fcc Monte Carlo simulation may be also attributed to phonon and/or magnetic entropy contributions not included into simulation.

At  $x_{\text{Pd}} \geq 2/3$ ,  $\beta$ 2, and  $\beta$ 2-like structures are observed in simulation patterns at both high and low temperatures (below order-disorder transition), whereas the experimentally observed structure is L1<sub>2</sub>.<sup>5</sup> Moreover, the temper-

ature  $T_{\text{ord}} = 832$  K obtained in the simulation at  $x_{\text{Pd}} = 2/3$  is considerably lower than the experimental  $T_{\text{ord}} = 1093$  K.

In order to confirm that there is no likelihood that the  $\beta$ 2-like Fe<sub>3</sub>Pd<sub>9</sub> (ID-4748) structure, identified here as the  $T = 0$  DFT ground state, could have been experimentally misinterpreted as L1<sub>2</sub>, we perform a simulation of diffractograms for the *ab initio* fully relaxed L1<sub>2</sub> and ID-4748 structures (see Fig. 12). The simulated L1<sub>2</sub> pattern compares well with the corresponding experimental diffractograms presented in Ref. 8. Figure 12 demonstrates that both FePd<sub>3</sub> (L1<sub>2</sub>) and Fe<sub>3</sub>Pd<sub>9</sub> (ID-4748) have five major peaks 111, 200, 220, 311, and 222. However, 200, 220, and 311 peaks in tetragonal Fe<sub>3</sub>Pd<sub>9</sub> (ID-4748) are triple-split. [Note that the same 200, 220, and 311 peaks in tetragonal FePd (L1<sub>0</sub>) are double-split.] These substantial

TABLE VIII. Same as Tables VI and VII but for bcc formation energies  $\Delta H = E(\sigma) - x_{\text{Fe}}E[\text{Fe,bcc}] - x_{\text{Pd}}E[\text{Pd,bcc}]$  (meV/atom) of DFT input structures used for Fe-Pd bcc cluster expansion. A2 means bcc.

ID	Stoich.	$x_{\text{Pd}}$	PR	Superlattice notation	$\Delta H$ DFT	$\Delta H$ CE	I
0	Fe	0.000	A2		0.0	-1.8	0
350	Fe <sub>7</sub> Pd	0.175	L1	None	43.0	42.5	0
11	Fe <sub>3</sub> Pd	0.250		(100)A <sub>3</sub> B	-2.1	3.5	0
14	Fe <sub>3</sub> Pd			(310)A <sub>3</sub> B	40.0	40.3	0
8	Fe <sub>3</sub> Pd			(211)A <sub>3</sub> B	42.7	43.7	0
6	Fe <sub>3</sub> Pd			(110)A <sub>3</sub> B	44.0	46.6	0
13	Fe <sub>3</sub> Pd		L6 <sub>0</sub>	None	57.4	58.5	0
10	Fe <sub>3</sub> Pd		L1 <sub>4</sub>	None	59.8	57.0	0
16	Fe <sub>3</sub> Pd		D0 <sub>3</sub>	(111)A <sub>3</sub> B	75.0	73.5	0
5	Fe <sub>2</sub> Pd	0.333	C11 <sub>b</sub>	(100)A <sub>2</sub> B	17.0	15.4	0
4	Fe <sub>2</sub> Pd			(111)A <sub>2</sub> B	82.9	82.6	0
90304	Fe <sub>10</sub> Pd <sub>6</sub>	0.375	L6	None	57.2	61.8	0
354	Fe <sub>5</sub> Pd <sub>3</sub>	0.375	L3	None	69.3	65.5	0
520	Fe <sub>5</sub> Pd <sub>4</sub>	0.444		None	-15.7	-16.1	4
246	Fe <sub>4</sub> Pd <sub>4</sub>	0.500		None	-39.9	-43.7	1
353	Fe <sub>4</sub> Pd <sub>4</sub>		L4	None	27.8	25.8	0
17	Fe <sub>2</sub> Pd <sub>2</sub>		B32	(111)A <sub>2</sub> B <sub>2</sub>	44.0	44.1	0
354	Fe <sub>3</sub> Pd <sub>5</sub>	0.625	L5	None	0.8	2.3	0
90304	Fe <sub>6</sub> Pd <sub>10</sub>	0.625	L10	None	6.8	5.0	0
5	FePd <sub>2</sub>	0.667	C11 <sub>b</sub>	(100)AB <sub>2</sub>	-95.9	-92.5	0*
4	FePd <sub>2</sub>	0.667		(111)AB <sub>2</sub>	-63.5	-61.8	0
16	FePd <sub>3</sub>	0.750	D0 <sub>3</sub>	(111)AB <sub>3</sub>	-46.8	-46.5	0
10	FePd <sub>3</sub>	0.750	L1 <sub>4</sub>	None	1.5	4.1	0
622	Fe <sub>2</sub> Pd <sub>7</sub>	0.778		(421)AB <sub>2</sub> AB <sub>5</sub>	-54.3	-55.4	3
578	Fe <sub>2</sub> Pd <sub>7</sub>			(111)A <sub>2</sub> B <sub>7</sub>	-12.2	-11.7	1
29	FePd <sub>4</sub>	0.800		(111)AB <sub>4</sub>	-43.0	-43.6	1
77	FePd <sub>5</sub>	0.833		(111)AB <sub>5</sub>	-38.1	-44.7	1
90944	Fe <sub>2</sub> Pd <sub>14</sub>	0.875		None	-28.3	-30.8	2
350	FePd <sub>7</sub>		L7	None	-13.9	-12.8	0
619	FePd <sub>8</sub>	0.889		(124)AB <sub>8</sub>	-46.2	-42.0	1*
90943	FePd <sub>15</sub>	0.938		None	-18.0	-18.7	2
0	Pd	1.000	A2		0.0	1.2	0

differences leave no room for interpretation of the tetragonal ID-4748 as cubic FePd<sub>3</sub> (L1<sub>2</sub>).

It is possible that the DFT-predicted tendency for  $\beta 2$  ordering could be detected at higher temperatures in diffuse scattering experiments. Unfortunately, we can not find experimental measurements of the diffuse scattering from substitutionally disordered single crystal at these compositions to compare with our results.

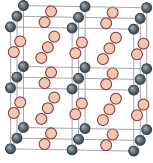
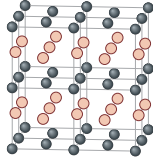
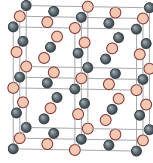
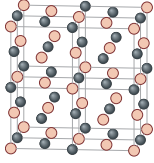
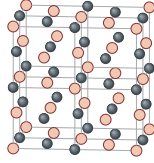
## VI. CONCLUSIONS

In this paper, we perform a first-principles mixed-basis cluster expansion for fcc and bcc Fe-Pd alloys. The leading pair and many-body interactions controlling energetic and thermodynamic phase stability in this system are distilled via genetic algorithm selection. The input set of  $\sim 100$  structures is altered iteratively in order to obtain a self-consistent solution to the cluster expansion representation. Structures are relaxed without symmetry constraints as fcc-based compounds often revert to bcc/bct-like structures upon relaxation and vice versa. We use the structural and magnetic “filters,” determining whether a fully relaxed structure is of fcc/bcc and

high-/low-spin types for use it in the corresponding cluster expansion. Our cluster expansions demonstrate the following features.

In the Fe-rich composition range (see Fig. 7), a fcc-only cluster expansion reveals a single (except fcc Fe) ground state L1<sub>0</sub>, whereas a bcc-only cluster expansion reveals no ground states (except bcc Fe). However, L1<sub>0</sub> structure is higher in energy than the phase separation into bcc Fe/fcc FePd<sub>2</sub>( $\beta 2$ ). If such (incoherent) phase separation were kinetically slow, fcc L1<sub>0</sub> would be observed at low temperatures. At higher temperatures, the experimental observation of bcc $\rightarrow$ fcc transition of iron suggests the increase of bcc-Fe free energy over fcc Fe due to the phonon and/or magnetic entropy contributions. If the same tendency keeps for Fe-rich compounds, the transformation from ground phase separation bcc Fe/FePd<sub>2</sub>( $\beta 2$ ) into bcc Fe/FePd(L1<sub>0</sub>) is expected with increase of temperature at  $x_{\text{Pd}} \leq 0.50$  in accordance with the experimental phase diagram. The comparatively low L1<sub>0</sub>/disorder transition temperature obtained by fcc Monte Carlo simulation (see Fig. 11) may be also attributed to phonon and/or magnetic entropy contributions not included into simulation. We further find that the bcc random alloy

TABLE IX. (Color online) Fcc structures corresponding the high-symmetry (Lifshitz)  $\mathbf{k}$  points and described by one order parameter. All coordinates are cartesian.

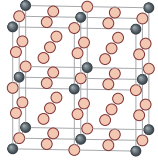
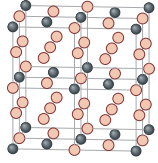
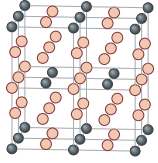
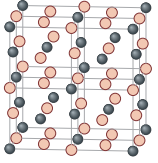
Structure ID	L1 <sub>2</sub> (A <sub>3</sub> B; AB <sub>3</sub> ) 15	L1 <sub>0</sub> (AB) 1	L1 <sub>1</sub> (AB) 2	D4 (A <sub>4</sub> B <sub>4</sub> ) 373	CH, "40" (A <sub>2</sub> B <sub>2</sub> ) 17
Prototypes	Cu <sub>3</sub> Au 	CuAu-I 	CuPt 		NbP 
Bravais lattice	Simple cubic	Simple tetragonal	Rhombohedral (trigonal)	Face-centered cubic	Body-centered tetragonal
Unit cell basis	(1,0,0) (0,1,0)	( $\frac{1}{2}, \frac{1}{2}, 0$ ) ( $\frac{1}{2}, \frac{1}{2}, 0$ )	( $\frac{1}{2}, \frac{1}{2}, 0$ ) ( $\frac{1}{2}, 0, \frac{1}{2}$ )	(1,1,0) (1, $\bar{1}$ ,0)	(1,0,0) (0,1,0)
vectors	(0,0,1)	(0,0,1)	(1, $\frac{1}{2}, \frac{1}{2}$ )	(1,0, $\bar{1}$ )	( $\frac{1}{2}, \frac{1}{2}, 1$ )
Atomic positions in unit cell (compl. ord.)	A:(0,0,0) B:( $\frac{1}{2}, \frac{1}{2}, 0$ ) B:( $\frac{1}{2}, 0, \frac{1}{2}$ ) B:(0, $\frac{1}{2}, \frac{1}{2}$ )	A:(0,0,0) B:(0, $\frac{1}{2}, \frac{1}{2}$ )	A:(0,0,0) B:(1,0,0)	A:(0,0,0) A:( $\frac{1}{2}, \frac{1}{2}, 0$ ) A:( $\frac{3}{2}, 0, \frac{1}{2}$ ) A:(1, $\frac{1}{2}, \frac{1}{2}$ ) B:(1, $\frac{1}{2}, \frac{1}{2}$ ) B:( $\frac{1}{2}, 0, \frac{1}{2}$ ) B:( $\frac{1}{2}, \frac{1}{2}, 0$ ) B:(1,0,0)	A:(0,0,0) A:( $\frac{1}{2}, 1, \frac{1}{2}$ ) B:( $\frac{1}{2}, \frac{1}{2}, 0$ ) B:(1, $\frac{1}{2}, \frac{1}{2}$ )
Superlattice (compl. ord.)	None	A <sub>1</sub> B <sub>1</sub> [001]	A <sub>1</sub> B <sub>1</sub> [111]	None	A <sub>2</sub> B <sub>2</sub> [201]
Space group Int. Tab. <sup>47</sup>	Pm $\bar{3}$ m(221)	P4/mmm(123)	R $\bar{3}$ m(166)	Fd $\bar{3}$ m(227)	I4 <sub>1</sub> /amd(141)
Shoenflies	O <sub>h</sub> <sup>1</sup>	D <sub>4h</sub> <sup>1</sup>	D <sub>3d</sub> <sup>5</sup>	O <sub>h</sub> <sup>7</sup>	D <sub>4h</sub> <sup>19</sup>
Pearson	cP4	tP4	hR32		tI8
Probability distribution function $P_{\mathbf{R}}$ (part. ord.)	$x + \frac{1}{4}\eta_X[\exp(i\mathbf{k}_{X_1}\mathbf{R}) + \exp(i\mathbf{k}_{X_2}\mathbf{R}) + \exp(i\mathbf{k}_{X_3}\mathbf{R})]$	$x + \frac{1}{2}\eta_X \exp(i\mathbf{k}_{X_1}\mathbf{R})$	$x + \frac{1}{2}\eta_L \exp(i\mathbf{k}_{L_1}\mathbf{R})$	$x + \frac{1}{4}\eta_L \times [-\exp(i\mathbf{k}_{L_1}\mathbf{R}) + \exp(i\mathbf{k}_{L_2}\mathbf{R}) + \exp(i\mathbf{k}_{L_3}\mathbf{R}) + \exp(i\mathbf{k}_{L_4}\mathbf{R})]$	$x + \frac{1}{2}\eta_W[\sin \mathbf{k}_{W_1}\mathbf{R} + \cos \mathbf{k}_{W_2}\mathbf{R}]$
$P_1$	$x + \frac{3}{4}\eta_X$ (1)	$x + \frac{1}{2}\eta_X$ (1)	$x + \frac{1}{2}\eta_L$ (1)	$x + \frac{1}{2}\eta_L$ (4)	$x + \frac{1}{2}\eta_W$ (2)
$P_2$	$x - \frac{1}{4}\eta_X$ (3)	$x - \frac{1}{2}\eta_X$ (1)	$x - \frac{1}{2}\eta_L$ (1)	$x - \frac{1}{2}\eta_L$ (4)	$x - \frac{1}{2}\eta_W$ (2)

mixing enthalpy is positive and has negative second derivative in this composition range, indicating a tendency to spinodal decomposition. Thus bcc structures are not expected to appear in Fe-rich composition range even at moderate temperatures.

In the Pd-rich composition range (see Fig. 7), the bcc-only cluster expansion shows two ground states: FePd<sub>2</sub> (C11<sub>b</sub>) and (124) bcc superlattice FePd<sub>8</sub>. However, none of the bcc compounds are ground states if take into account the competition from the obtained fcc ground states: FePd<sub>2</sub> ( $\beta_2$ ), Fe<sub>3</sub>Pd<sub>9</sub>, Fe<sub>2</sub>Pd<sub>7</sub>, FePd<sub>5</sub>, Fe<sub>2</sub>Pd<sub>13</sub>, and FePd<sub>8</sub>. (100) fcc superlattice FePd<sub>2</sub> ( $\beta_2$ ) is the deepest ground state in the entire compositional range of Fe-Pd. All the other five ground states with higher palladium contents are the derivatives of FePd<sub>2</sub>

( $\beta_2$ ) obtained by substitution of some iron atoms by palladium in order to account for a different stoichiometry. [The bcc-only ground state FePd<sub>2</sub> (C11<sub>b</sub>) is also crystallographically equivalent (differing only by the value of the  $c/a$  ratio) to fcc FePd<sub>2</sub> ( $\beta_2$ ).] We find that the L1<sub>2</sub> fcc structure detected experimentally for FePd<sub>3</sub> at higher temperatures is not a  $T = 0$  ground state, since the energy of newly discovered Fe<sub>3</sub>Pd<sub>9</sub> fcc structure is lower by  $\sim 5$  meV/atom than that of L1<sub>2</sub>. The fcc Monte Carlo simulation does not reveal the secondary phase transitions from  $\beta_2$ -like structures into L1<sub>2</sub> (see Fig. 11). All  $\beta_2$ -like structures transform directly into the disordered state at temperatures that are lower than those measured experimentally for L1<sub>2</sub>/disorder transitions. However, the simulated transition temperatures are high enough

TABLE X. (Color online) Fcc structures corresponding the high-symmetry (Lifshitz)  $\mathbf{k}$  points and described by two order parameters. All coordinates are cartesian.

Structure ID	D1 (A <sub>7</sub> B); D7 (AB <sub>7</sub> ) 371	L1 <sub>3</sub> (A <sub>3</sub> B; AB <sub>3</sub> ) 10	DO <sub>22</sub> (A <sub>3</sub> B; AB <sub>3</sub> ) 16	D3 (A <sub>5</sub> B <sub>3</sub> ); D5(A <sub>3</sub> B <sub>5</sub> ) 372
Prototypes	CuPt <sub>7</sub> , Ca <sub>7</sub> Ge 	CuPt <sub>3</sub> 		
Bravais lattice	Face-centered cubic	Base-centered orthorhombic	Body-centered tetragonal	Rhombohedral (trigonal)
Unit cell	(1,1,0)	( $\frac{1}{2}, \frac{1}{2}, 0$ )	(1,0,0)	(1,1,0)
basis	(1, $\bar{1}$ , 0)	( $\frac{1}{2}, \frac{1}{2}, 1$ )	(0,1,0)	(1, $\bar{1}$ , 0)
vectors	(1,0, $\bar{1}$ )	( $\frac{1}{2}, \frac{1}{2}, \bar{1}$ )	( $\frac{1}{2}, \frac{1}{2}, 1$ )	(1,0, $\bar{1}$ )
Atomic positions	A:(0,0,0), B:(1,0,0) B:( $\frac{3}{2}, 0, \frac{1}{2}$ ), B:( $1, \frac{1}{2}, \frac{1}{2}$ )	A:(0,0,0) B:( $\frac{1}{2}, \frac{1}{2}, 0$ )	A:(0,0,0) B:( $\frac{1}{2}, \frac{1}{2}, 0$ )	A:(0,0,0), A:( $\frac{1}{2}, \frac{1}{2}, 0$ ) A:( $\frac{3}{2}, 0, \frac{1}{2}$ ), B:( $\frac{1}{2}, 0, \frac{1}{2}$ )
in unit cell	B:( $1, \frac{1}{2}, \frac{1}{2}$ ), B:( $\frac{1}{2}, 0, \frac{1}{2}$ )	B:( $\frac{1}{2}, 0, \frac{1}{2}$ )	B:( $\frac{1}{2}, 1, \frac{1}{2}$ )	B:( $\frac{1}{2}, \frac{1}{2}, 0$ ), B:(1,0,0)
(compl. ord.)	B:( $\frac{1}{2}, \frac{1}{2}, 0$ ), B:( $\frac{1}{2}, \frac{1}{2}, 0$ )	B:( $\frac{1}{2}, 0, \frac{1}{2}$ )	B:( $1, \frac{1}{2}, \frac{1}{2}$ )	B:( $1, \frac{1}{2}, \frac{1}{2}$ ), B:( $1, \frac{1}{2}, \frac{1}{2}$ )
Superlattice (compl. ord.)	None	None	A <sub>3</sub> B along [201]	None
Space group	Fm $\bar{3}$ m(225)	Cmmm(65)	I4/mmm (139)	R $\bar{3}$ m(166)
Int. Tab. <sup>47</sup>	Fm $\bar{3}$ m(225)	Cmmm(65)	I4/mmm (139)	R $\bar{3}$ m(166)
Shoenflies	O <sub>h</sub> <sup>5</sup>	D <sub>2h</sub> <sup>19</sup>	D <sub>4h</sub> <sup>17</sup>	D <sub>3d</sub> <sup>5</sup>
Pearson	cF32	cF4	tI8	
Probability distribution function $P_{\mathbf{R}}$	$x + \frac{1}{8}\eta_X[\exp(i\mathbf{k}_{X_1}\mathbf{R}) + \exp(i\mathbf{k}_{X_2}\mathbf{R}) + \exp(i\mathbf{k}_{X_3}\mathbf{R})] + \frac{1}{8}\eta_L[\exp(i\mathbf{k}_{L_1}\mathbf{R}) + \exp(i\mathbf{k}_{L_2}\mathbf{R}) + \exp(i\mathbf{k}_{L_3}\mathbf{R}) + \exp(i\mathbf{k}_{L_4}\mathbf{R})]$	$x + \frac{1}{4}\eta_X \exp(i\mathbf{k}_{X_1}\mathbf{R}) + \frac{1}{4}\eta_L[\exp(i\mathbf{k}_{L_1}\mathbf{R}) + \exp(i\mathbf{k}_{L_4}\mathbf{R})]$	$x + \frac{1}{4}\eta_X \exp(i\mathbf{k}_{X_1}\mathbf{R}) + \frac{1}{4}\eta_W[\exp(i\mathbf{k}_{W_1}\mathbf{R}) + \exp(i\mathbf{k}_{W_2}\mathbf{R})]$	$x + \frac{1}{8}\eta_X[-\exp(i\mathbf{k}_{X_1}\mathbf{R}) + \exp(i\mathbf{k}_{X_2}\mathbf{R}) + \exp(i\mathbf{k}_{X_3}\mathbf{R})] + \frac{1}{8}\eta_L[-\exp(i\mathbf{k}_{L_1}\mathbf{R}) + \exp(i\mathbf{k}_{L_2}\mathbf{R}) + \exp(i\mathbf{k}_{L_3}\mathbf{R}) + 3\exp(i\mathbf{k}_{L_4}\mathbf{R})]$
$P_1$	$x + \frac{3}{8}\eta_X + \frac{1}{2}\eta_L$ (1)	$x - \frac{1}{4}\eta_X - \frac{1}{2}\eta_L$ (1)	$x + \frac{1}{4}\eta_X + \frac{1}{2}\eta_W$ (1)	$x + \frac{1}{8}\eta_X + \frac{1}{2}\eta_L$ (3)
$P_2$	$x + \frac{3}{8}\eta_X - \frac{1}{2}\eta_L$ (1)	$x - \frac{1}{4}\eta_X + \frac{1}{2}\eta_L$ (1)	$x + \frac{1}{4}\eta_X - \frac{1}{2}\eta_W$ (1)	$x + \frac{1}{8}\eta_X - \frac{1}{2}\eta_L$ (3)
$P_3$	$x - \frac{1}{8}\eta_X$ (6)	$x + \frac{1}{4}\eta_X$ (2)	$x - \frac{1}{4}\eta_X$ (2)	$x - \frac{3}{8}\eta_X$ (2)
Atomic positions	$P_1:(0,0,0), P_2:(1,0,0)$ $P_3:(\frac{3}{2}, 0, \frac{1}{2}), P_3:(1, \frac{1}{2}, \frac{1}{2})$	$P_1:(0,0,0)$ $P_2:(\frac{1}{2}, \frac{1}{2}, 0)$	$P_1:(0,0,0)$ $P_2:(\frac{1}{2}, \frac{1}{2}, 0)$	$P_1:(0,0,0), P_1:(\frac{1}{2}, \frac{1}{2}, 0)$ $P_1:(\frac{3}{2}, 0, \frac{1}{2}), P_2:(\frac{1}{2}, 0, \frac{1}{2})$
in the unit cell	$P_3:(1, \frac{1}{2}, \frac{1}{2}), P_3:(\frac{1}{2}, 0, \frac{1}{2})$	$P_3:(\frac{1}{2}, 0, \frac{1}{2})$	$P_3:(\frac{1}{2}, 1, \frac{1}{2})$	$P_2:(\frac{1}{2}, \frac{1}{2}, 0), P_2:(1,0,0)$
(part. ord.)	$P_3:(\frac{1}{2}, \frac{1}{2}, 0), P_3:(\frac{1}{2}, \frac{1}{2}, 0)$	$P_3:(\frac{1}{2}, 0, \frac{1}{2})$	$P_3:(1, \frac{1}{2}, \frac{1}{2})$	$P_3:(1, \frac{1}{2}, \frac{1}{2}), P_3:(1, \frac{1}{2}, \frac{1}{2})$

for an experimental stabilization of these structures to be possible.

We consider our determination of ground states results as robust within the utilized DFT-GGA framework. The general DFT tendency to  $\beta 2$ -like structures at  $x_{Pd} \geq 2/3$  eliminates the possibility of DFT error for just some structures. Besides, the energy difference between L1<sub>2</sub> and the DFT ground state of the same stoichiometry is more than the estimated error of our DFT calculations. Note that similarly to Fe-Pd, the deep  $\beta 2$  ground state has been obtained in Cu-Au,<sup>53</sup> Fe-Pt (ferromagnetic),<sup>7</sup> and Co-Pt<sup>54</sup> from first principles despite

the experimentally observed L1<sub>2</sub> in these alloys at finite temperatures.

At finite temperatures, the free-energy contributions from configurational (substitutional), phonon, and magnetic excitations may stabilize structures that are different from  $T = 0$  ground states. The configurational entropy is already included in the Monte Carlo simulation. So we suggest that phonons and magnetic disorder are responsible for the experimentally observed L1<sub>2</sub> structure at finite temperatures. An additional study of such effects is thus highly desirable.

TABLE XI. (Color online) Bcc structures corresponding the high-symmetry (Lifshitz)  $\mathbf{k}$  points and described by one order parameter. All coordinates are cartesian.

Structure ID	B2 (AB) 2	B32 (A <sub>2</sub> B <sub>2</sub> ) 17	L1 <sub>4</sub> (A <sub>3</sub> B;AB <sub>3</sub> ) 10	A <sub>1</sub> (AB) 1	L4 (A <sub>4</sub> B <sub>4</sub> ) 353
Prototypes	CsCl, $\beta$ -CuZn	NaTa		$\gamma$ -IrV, Ta <sub>2</sub> O	
Bravais lattice	Simple cubic	Face-centered cubic	Rhombohedral (trigonal)	Face-centered orthorhombic	Body-centered tetragonal
Unit cell basis vectors	(1,0,0) (0,1,0) (0,0,1)	(0,1,1) (1,0,1) (1,1,0)	$(\frac{1}{2}, \frac{1}{2}, \frac{1}{2})$ $(\frac{3}{2}, \frac{1}{2}, \frac{1}{2})$ (1,1, $\bar{1}$ )	$(\frac{1}{2}, \frac{1}{2}, \frac{1}{2})$ $(\frac{1}{2}, \frac{1}{2}, \frac{1}{2})$ $(\bar{1}, 1, 0)$	(1,1,1) (1,1, $\bar{1}$ ) (0,2,0)
Atomic positions in unit cell (compl. ord.)	A:(0,0,0) B:( $\frac{1}{2}, \frac{1}{2}, \frac{1}{2}$ )	A:(0,0,0) A:( $\frac{1}{2}, \frac{1}{2}, \frac{1}{2}$ ) B:(0,0,1) B:( $\frac{1}{2}, \frac{1}{2}, \frac{3}{2}$ )	A:(0,0,0) B:( $\frac{1}{2}, \frac{1}{2}, \frac{1}{2}$ ) B:( $\frac{3}{2}, \frac{1}{2}, \frac{1}{2}$ ) B:(1,0,0)	A:(0,0,0) B:(0,1,0)	A:(0,0,0) A:( $\frac{1}{2}, \frac{1}{2}, \frac{1}{2}$ ) A:(1,2,0) A:( $\frac{1}{2}, \frac{3}{2}, \frac{1}{2}$ ) B:( $\frac{1}{2}, \frac{3}{2}, \frac{1}{2}$ ) B:(0,1,0) B:(1,1,0) B:( $\frac{1}{2}, \frac{1}{2}, \frac{1}{2}$ )
Superlattice (compl. ord.)	A <sub>1</sub> B <sub>1</sub> [001]	A <sub>2</sub> B <sub>2</sub> [111]	None	A <sub>1</sub> B <sub>1</sub> [101]	None
Space group Int. Tab. <sup>47</sup>	Pm $\bar{3}$ m(221)	Fd $\bar{3}$ m(227)	R $\bar{3}$ m(166)	Cmmm(65)	I4 <sub>1</sub> /amd(141)
Shoenflies	O <sub>h</sub> <sup>1</sup>	O <sub>h</sub> <sup>7</sup>	D <sub>3d</sub> <sup>5</sup>	D <sub>2h</sub> <sup>19</sup>	D <sub>4h</sub> <sup>19</sup>
Pearson	cP2	cF16		oC8	
Probability	x+	x+	x+	x+	x+
distribution function $P_{\mathbf{R}}$ (part. ord.)	$\frac{1}{2}\eta_H \cos(\mathbf{k}_H \mathbf{R})$	$\frac{1}{2}\eta_P [\sin(\mathbf{k}_{P_1} \mathbf{R}) + \cos(\mathbf{k}_{P_2} \mathbf{R})]$	$\frac{1}{4}\eta_N [\cos(\mathbf{k}_{N_4} \mathbf{R}) + \cos(\mathbf{k}_{N_5} \mathbf{R}) + \cos(\mathbf{k}_{N_6} \mathbf{R})]$	$\frac{1}{2}\eta_N \cos(\mathbf{k}_{N_3} \mathbf{R})$	$\frac{1}{4}\eta_N [\cos(\mathbf{k}_{N_3} \mathbf{R}) - \cos(\mathbf{k}_{N_2} \mathbf{R}) + \cos(\mathbf{k}_{N_5} \mathbf{R}) + \cos(\mathbf{k}_{N_6} \mathbf{R})]$
$P_1$	$x + \frac{1}{2}\eta_H$ (1)	$x + \frac{1}{2}\eta_P$ (2)	$x + \frac{3}{4}\eta_N$ (1)	$x + \frac{1}{2}\eta_N$ (1)	$x + \frac{1}{2}\eta_N$ (4)
$P_2$	$x - \frac{1}{2}\eta_H$ (1)	$x - \frac{1}{2}\eta_P$ (2)	$x - \frac{1}{4}\eta_N$ (3)	$x - \frac{1}{2}\eta_N$ (1)	$x - \frac{1}{2}\eta_N$ (4)

## ACKNOWLEDGMENTS

This work has started while the authors were at the National Renewable Energy Laboratory and was funded there by US DOE, Office of Science, Basic Energy Science, under Contract No. DEAC36-98-GO10337.

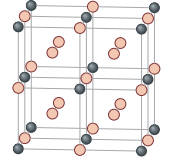
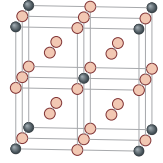
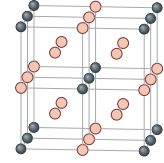
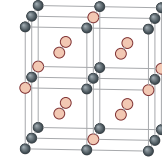
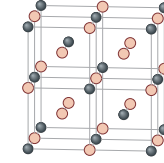
## APPENDIX A: PSEUDOPOTENTIAL VERSUS ALL-ELECTRON

A verification of the systematic error associated with the use of pseudopotentials rather than all-electron (FLAPW) is done in Tables IV and V for pure iron and palladium as well as for some of their compounds. We conclude the following.

The agreement for magnetic moment, lattice parameter, and values of  $E[\text{Fe}, \text{fcc-LS}] - E[\text{Fe}, \text{bcc}]$  and  $E[\text{Fe}, \text{fcc-HS}] - E[\text{Fe}, \text{bcc}]$  is good for pure solid elements and compounds, especially taking into account the scatter in FLAPW results obtained from different references. (The scatter may be attributed to the different  $k$  mesh and energy cutoff parameters used by different authors, see footnotes in Table IV).

In case of L1<sub>2</sub> Fe<sub>3</sub>Pd and L1<sub>0</sub> FePd compounds (see Table V), the pseudopotential formation energies differ considerably from those calculated within LAPW by Mohri *et al.*<sup>31</sup> It is possible that such a difference is caused by insufficient  $k$  mesh and energy cutoff parameters used in Ref. 31. For example, the results of Ref. 31 in the case of Fe-Ni alloy (with the same  $k$  mesh and energy cutoff parameters as in Fe-Pd) differ from those of Ref. 32 (LAPW but with much higher  $k$  mesh and energy cutoff) by 7, 20, 13, 55,

TABLE XII. (Color online) Bcc structures corresponding the high-symmetry (Lifshitz)  $\mathbf{k}$  points and described by two and three order parameters. All coordinates are cartesian.

Structure ID	D0 <sub>3</sub> (A <sub>3</sub> B;AB <sub>3</sub> ) 16	L1(A <sub>7</sub> B);L7(AB <sub>7</sub> ) 350	L6 <sub>0</sub> (A <sub>3</sub> B;AB <sub>3</sub> ) 13	L3(A <sub>5</sub> B <sub>3</sub> );L5(A <sub>3</sub> B <sub>5</sub> ) 354	L6(A <sub>10</sub> B <sub>6</sub> );L10(A <sub>6</sub> B <sub>10</sub> ) 90304
Prototypes	Fe <sub>3</sub> Al,BiF <sub>3</sub> ,Cs <sub>3</sub> Sb 	Fe <sub>8</sub> N 	CuTi <sub>3</sub> ,Ta <sub>4</sub> O 		
Bravais lattice	Face-centered cubic	Body-centered cubic	Simple tetragonal	Body-centered cubic	Simple cubic
Basis vectors	(110)(1 $\bar{1}$ 0)(10 $\bar{1}$ )	(111)(11 $\bar{1}$ )(020)	(100)(011)(0 $\bar{1}$ 1)	(111)(11 $\bar{1}$ )(020)	(200)(020)(002)
Atomic positions	A(000) B(100)	A(000),B(110) B(010),B(120)	A(000) B(001)	A(000),A(120) A(010),B(110)	A(000),A(110),A( $\frac{3}{2}\frac{1}{2}\frac{1}{2}$ ) A(101),A(011),A( $\frac{1}{2}\frac{1}{2}\frac{3}{2}$ )
in unit cell	B( $\frac{3}{2}\frac{1}{2}\frac{1}{2}$ )	B( $\frac{1}{2}\frac{3}{2}\frac{1}{2}$ ),B( $\frac{1}{2}\frac{3}{2}\frac{1}{2}$ )	B( $\frac{1}{2}\frac{1}{2}\frac{1}{2}$ )	B( $\frac{1}{2}\frac{3}{2}\frac{1}{2}$ ),B( $\frac{1}{2}\frac{3}{2}\frac{1}{2}$ )	B(010),B(100),B( $\frac{1}{2}\frac{1}{2}\frac{1}{2}$ )
(compl. ord.)	B( $\frac{3}{2}\frac{1}{2}\frac{1}{2}$ )	B( $\frac{1}{2}\frac{1}{2}\frac{1}{2}$ ),B( $\frac{1}{2}\frac{1}{2}\frac{1}{2}$ )	B( $\frac{1}{2}\frac{1}{2}\frac{1}{2}$ )	B( $\frac{1}{2}\frac{1}{2}\frac{1}{2}$ ),B( $\frac{1}{2}\frac{1}{2}\frac{1}{2}$ )	B(111),B(001),B( $\frac{1}{2}\frac{3}{2}\frac{3}{2}$ ) B( $\frac{3}{2}\frac{1}{2}\frac{1}{2}$ ),B( $\frac{3}{2}\frac{1}{2}\frac{1}{2}$ ) B( $\frac{3}{2}\frac{1}{2}\frac{3}{2}$ ),B( $\frac{3}{2}\frac{3}{2}\frac{3}{2}$ )
Superlattice	A <sub>3</sub> B <sub>1</sub> along [111]	None	None	None	None
Space group	Fm $\bar{3}$ m(225)	Im $\bar{3}$ m (229)	P4/mmm (123)	Im $\bar{3}$ m (229)	Pn $\bar{3}$ m (224)
Int. Tab. <sup>47</sup>	Fm $\bar{3}$ m(225)	Im $\bar{3}$ m (229)	P4/mmm (123)	Im $\bar{3}$ m (229)	Pn $\bar{3}$ m (224)
Shoenflies	O <sub>h</sub> <sup>5</sup>	O <sub>h</sub> <sup>9</sup>	D <sub>4h</sub> <sup>1</sup>	O <sub>h</sub> <sup>9</sup>	O <sub>h</sub> <sup>4</sup>
Pearson	cF16		tP4		
Probability distribution function $P_{\mathbf{R}}$	$x + \frac{1}{4}\eta_H \cos(\mathbf{k}_H \mathbf{R}) + \frac{1}{4}\eta_P [\exp(i\mathbf{k}_{P_1} \mathbf{R}) + \exp(i\mathbf{k}_{P_2} \mathbf{R})]$	$x + \frac{1}{8}\eta_H \cos(\mathbf{k}_H \mathbf{R}) + \frac{1}{8}\eta_N [\exp(i\mathbf{k}_{N_1} \mathbf{R}) + \exp(i\mathbf{k}_{N_2} \mathbf{R}) + \exp(i\mathbf{k}_{N_3} \mathbf{R}) + \exp(i\mathbf{k}_{N_4} \mathbf{R}) + \exp(i\mathbf{k}_{N_5} \mathbf{R}) + \exp(i\mathbf{k}_{N_6} \mathbf{R})]$	$x + \frac{1}{4}\eta_H \cos(\mathbf{k}_H \mathbf{R}) + \frac{1}{4}\eta_N [\cos(\mathbf{k}_{N_1} \mathbf{R}) + \cos(\mathbf{k}_{N_4} \mathbf{R})]$	$x + \frac{3}{8}\eta_H \cos(\mathbf{k}_H \mathbf{R}) - \frac{1}{8}\eta_N [\exp(i\mathbf{k}_{N_1} \mathbf{R}) + \exp(i\mathbf{k}_{N_2} \mathbf{R}) + \exp(i\mathbf{k}_{N_3} \mathbf{R}) + \exp(i\mathbf{k}_{N_4} \mathbf{R}) + \exp(i\mathbf{k}_{N_5} \mathbf{R}) + \exp(i\mathbf{k}_{N_6} \mathbf{R})]$	$x + \frac{1}{8}\eta_H \cos(\mathbf{k}_H \mathbf{R}) + \frac{1}{4}\eta_P [\exp(i\mathbf{k}_{P_1} \mathbf{R}) + \exp(i\mathbf{k}_{P_2} \mathbf{R})] + \frac{1}{8}\eta_N [-\cos(\mathbf{k}_{N_1} \mathbf{R}) - \cos(\mathbf{k}_{N_2} \mathbf{R}) - \cos(\mathbf{k}_{N_3} \mathbf{R}) + \cos(\mathbf{k}_{N_4} \mathbf{R}) + \cos(\mathbf{k}_{N_5} \mathbf{R}) + \cos(\mathbf{k}_{N_6} \mathbf{R})]$
$P_1$	$x + \frac{1}{4}\eta_H - \frac{1}{2}\eta_P$ (1)	$x + \frac{1}{8}\eta_H + \frac{3}{4}\eta_N$ (1)	$x + \frac{1}{4}\eta_H + \frac{1}{2}\eta_N$ (1)	$x + \frac{3}{8}\eta_H + \frac{1}{4}\eta_N$ (3)	$x + \frac{1}{8}\eta_H + \frac{1}{2}\eta_P$ (4)
$P_2$	$x + \frac{1}{4}\eta_H + \frac{1}{2}\eta_P$ (1)	$x + \frac{1}{8}\eta_H - \frac{1}{4}\eta_N$ (3)	$x + \frac{1}{4}\eta_H - \frac{1}{2}\eta_N$ (1)	$x + \frac{3}{8}\eta_H - \frac{3}{4}\eta_N$ (1)	$x - \frac{1}{8}\eta_H + \frac{3}{4}\eta_N$ (2)
$P_3$	$x - \frac{1}{4}\eta_H$ (2)	$x - \frac{1}{8}\eta_H$ (4)	$x - \frac{1}{4}\eta_H$ (2)	$x - \frac{3}{8}\eta_H$ (4)	$x + \frac{1}{8}\eta_H - \frac{1}{2}\eta_P$ (4)
$P_4$					$x - \frac{1}{8}\eta_H - \frac{1}{4}\eta_N$ (6)
Atomic positions	P <sub>1</sub> (000) P <sub>2</sub> (100)	P <sub>1</sub> (000),P <sub>2</sub> (110) P <sub>2</sub> (010),P <sub>2</sub> (120)	P <sub>1</sub> (000) P <sub>2</sub> (001)	P <sub>1</sub> (000),P <sub>1</sub> (120) P <sub>1</sub> (010),P <sub>2</sub> (110)	P <sub>1</sub> (000),P <sub>1</sub> (110),P <sub>2</sub> ( $\frac{3}{2}\frac{3}{2}\frac{1}{2}$ ) P <sub>1</sub> (101),P <sub>1</sub> (011),P <sub>2</sub> ( $\frac{1}{2}\frac{1}{2}\frac{3}{2}$ )
in the unit cell	P <sub>3</sub> ( $\frac{3}{2}\frac{1}{2}\frac{1}{2}$ )	P <sub>3</sub> ( $\frac{1}{2}\frac{3}{2}\frac{1}{2}$ ),P <sub>3</sub> ( $\frac{1}{2}\frac{3}{2}\frac{1}{2}$ )	P <sub>3</sub> ( $\frac{1}{2}\frac{1}{2}\frac{1}{2}$ )	P <sub>3</sub> ( $\frac{1}{2}\frac{3}{2}\frac{1}{2}$ ),P <sub>3</sub> ( $\frac{1}{2}\frac{3}{2}\frac{1}{2}$ )	P <sub>3</sub> (010),P <sub>3</sub> (100),P <sub>4</sub> ( $\frac{1}{2}\frac{1}{2}\frac{1}{2}$ )
(part. ord.)	P <sub>3</sub> ( $\frac{3}{2}\frac{1}{2}\frac{1}{2}$ )	P <sub>3</sub> ( $\frac{1}{2}\frac{1}{2}\frac{1}{2}$ ),P <sub>3</sub> ( $\frac{1}{2}\frac{1}{2}\frac{1}{2}$ )	P <sub>3</sub> ( $\frac{1}{2}\frac{1}{2}\frac{1}{2}$ )	P <sub>3</sub> ( $\frac{1}{2}\frac{1}{2}\frac{1}{2}$ ),P <sub>3</sub> ( $\frac{1}{2}\frac{1}{2}\frac{1}{2}$ )	P <sub>3</sub> (111),P <sub>3</sub> (001),P <sub>4</sub> ( $\frac{1}{2}\frac{3}{2}\frac{3}{2}$ ) P <sub>4</sub> ( $\frac{3}{2}\frac{1}{2}\frac{1}{2}$ ),P <sub>4</sub> ( $\frac{1}{2}\frac{3}{2}\frac{1}{2}$ ) P <sub>4</sub> ( $\frac{3}{2}\frac{1}{2}\frac{3}{2}$ ),P <sub>4</sub> ( $\frac{3}{2}\frac{3}{2}\frac{3}{2}$ )

and 11 meV/atom for Fe(fcc-LS), L<sub>12</sub>(Fe<sub>3</sub>Ni), L<sub>10</sub>(FeNi), L<sub>11</sub>(FeNi), and L<sub>12</sub>(FeNi<sub>3</sub>), respectively.

In Table V, we also include the experimental data for high-temperature formation energies. In case of L<sub>12</sub> Fe<sub>3</sub>Pd and L<sub>10</sub> FePd compounds, the pseudopotential formation energies differ considerably from those obtained experimentally. Such a big difference is attributed to that the measurements were done for the disordered high-temperature state, whereas pseudopotential data correspond to the completely ordered states. The difference is substantially diminished when instead

of completely ordered states, we consider the random phase using cluster expansion (see Sec. III E).

### APPENDIX B: DFT INPUT DATA FOR Fe-Pd CLUSTER EXPANSIONS

Tables VI–VIII list the formation energies of all fully relaxed fcc and bcc DFT inputs for corresponding cluster expansions in Fe-Pd. Both DFT and fitted cluster expansion formation energies are listed.

### APPENDIX C: fcc STRUCTURES CORRESPONDING TO THE HIGH SYMMETRY (LIFSHITZ) POINTS IN THE RECIPROCAL SPACE

In case of fcc crystal lattice, the reciprocal space  $\mathbf{k}$  points corresponding to four stars  $\Gamma$ , X, L, and W satisfy Lifshitz criterion<sup>43,44</sup> being so-called high-symmetry  $\mathbf{k}$  points or Lifshitz points. The Lifshitz criterion requires that the point-group symmetries of such  $k$  points include intersecting symmetry elements. In other words,<sup>45</sup> any  $k$  direction can be reversed by some transformation from the own symmetry group of the high symmetry  $k$  point. Within the mean-field microscopic and macroscopic (phenomenological) approximations,<sup>43,44</sup> the structures corresponding to these high-symmetry  $\mathbf{k}$  points (Lifshitz structures) should be thermodynamically stable within a comparatively wide temperature-composition intervals, thus comprising large regions of the phase diagram.

The cartesian coordinates (in  $2\pi/a$  units, where  $a$  is an fcc lattice parameter) of fcc high-symmetry (Lifshitz) inequivalent  $\mathbf{k}$  points in the first Brillouin zone are the following:

$$\begin{aligned}\Gamma &= (0,0,0), \\ X_1 &= (0,0,1), \quad X_2 = (0,1,0), \quad X_3 = (1,0,0), \\ L_1 &= \left(\frac{1}{2}, \frac{1}{2}, \frac{1}{2}\right), \quad L_2 = \left(\frac{1}{2}, \frac{1}{2}, \bar{\frac{1}{2}}\right), \\ L_3 &= \left(\frac{1}{2}, \bar{\frac{1}{2}}, \frac{1}{2}\right), \quad L_4 = \left(\frac{1}{2}, \frac{1}{2}, \bar{\frac{1}{2}}\right), \\ W_1 &= \frac{1}{2}(2,0,1), \quad W_2 = -W_1, \quad W_3 = \frac{1}{2}(0,1,2), \\ W_4 &= -W_3, \quad W_5 = \frac{1}{2}(1,2,0), \quad W_6 = -W_5.\end{aligned}$$

In Ref. 46, the lists were completed for fcc and bcc structures described by the high-symmetry (Lifshitz)  $\mathbf{k}$  points

and having the correspondence of *one* order parameter to *one* star of  $\mathbf{k}$  vectors (i.e., to one irreducible representation of fcc or bcc space group). In Tables IX–X, such fcc complete list is presented. There,  $P_{\mathbf{R}}$  is one-atom probability distribution function equal to the probability of finding an A-type atom at crystal lattice site with radius vector  $\mathbf{R}$ . The order parameters are chosen to be zero in completely disordered state and all equal to unity in completely ordered state. The space groups of completely and partly ordered states are the same for each Lifshitz structure. The names D3 and D5 are chosen for structures having no prototype in literature.

### APPENDIX D: bcc STRUCTURES CORRESPONDING TO THE HIGH SYMMETRY (LIFSHITZ) POINTS IN THE RECIPROCAL SPACE

In case of bcc crystal lattice, the  $\mathbf{k}$  points corresponding to four stars  $\Gamma$ , H, P, and N satisfy Lifshitz criterion:

$$\begin{aligned}\Gamma &= (0,0,0), \\ H &= (0,0,1), \\ P_1 &= \left(\frac{1}{2}, \frac{1}{2}, \frac{1}{2}\right), \quad P_2 = \left(\bar{\frac{1}{2}}, \bar{\frac{1}{2}}, \bar{\frac{1}{2}}\right), \\ N_1 &= \left(0, \frac{1}{2}, \frac{1}{2}\right), \quad N_2 = \left(\frac{1}{2}, 0, \frac{1}{2}\right), \quad N_3 = \left(\frac{1}{2}, \frac{1}{2}, 0\right), \\ N_4 &= \left(0, \bar{\frac{1}{2}}, \frac{1}{2}\right), \quad N_5 = \left(\bar{\frac{1}{2}}, 0, \frac{1}{2}\right), \quad N_6 = \left(\bar{\frac{1}{2}}, \frac{1}{2}, 0\right).\end{aligned}$$

In Tables XI–XII, the complete list of bcc structures described by the high-symmetry (Lifshitz)  $\mathbf{k}$  points is presented.<sup>46</sup> The names L14, L4, L1, L7, L3, L5, L6, and L10 are chosen for structures having no prototype in literature.

\*Present address: Grandis, Inc., Milpitas, California 95035, USA.

†Present address: Intermolecular, Inc., San Jose, California 95134, USA.

<sup>1</sup>A. Kussmann and K. Müller, *Z. Angew. Phys.* **17**, 509 (1964); O. A. Ivanov, L. V. Solina, V. A. Demshila, and L. M. Magat, *Phys. Met. Metallogr.* **35**, 92 (1973).

<sup>2</sup>K. Sato, B. Bian, and Y. Hirotsu, *Jpn. J. Appl. Phys.* **39**, L1121 (2000); S. S. Kang, Z. Y. Jia, D. E. Nikles, and J. W. Harrell, *ibid.* **95**, 6744 (2004).

<sup>3</sup>T. Kakeshita and K. Ullakko, *MRS Bull.* **27**, 105 (2002).

<sup>4</sup>T. Hara, Y. Nakamura, and J. Nishimura, *Appl. Catal. A-Gen.* **320**, 144 (2007); J. Hong, F. Lan-Ying, Z. Hong, G. Zhi-Jun, and Z. Xin-Wei, *J. Inorg. Mater.* **23**, 847 (2008); S. Lee, M. H. Seo, S.-S. Cho, K.-H. Kang, J.-M. Kim, H. S. Hong, Y. Yun, and J.-H. Ahn, *Int. J. Mater. Res. Year* **99**, 1015 (2008); M. S. Yalfani, S. Contreras, J. Llorca, M. Dominguez, J. E. Sueiras, and F. Medina, *Phys. Chem. Chem. Phys.* **12**, 14673 (2010).

<sup>5</sup>*Binary Alloy Phase Diagrams*, edited by T. B. Massalski, H. Okamoto, P. K. Subramanian, and L. Kacprzak, 2nd ed. (American Society for Metals, Metals Park, OH, 1990).

<sup>6</sup>We do not consider the  $\delta$ -iron region in the present paper.

<sup>7</sup>S. V. Barabash, R. V. Chepulsii, V. Blum, and A. Zunger, *Phys. Rev. B* **80**, 220201 (2009).

<sup>8</sup>R. Hultgren and C. A. Zapffe, *Z. Kristallogr.* **99**, 509 (1938); C. A. Zapffe, Ph.D. theses, Harvard University, 1939.

<sup>9</sup>E. Raub, H. Beeskow, and O. Loebich, *Z. Metallkd.* **54**, 549 (1963); A. Kussmann and K. Jessen, *ibid.* **54**, 504 (1963).

<sup>10</sup>P. M. Marcus, F. Jona, and S. L. Qiu, *Phys. Rev. B* **66**, 064111 (2002).

<sup>11</sup>F. Jona and P. M. Marcus, *Phys. Rev. B* **65**, 155403 (2002).

<sup>12</sup>L. G. Wang, M. Šob, and Z. Zhang, *J. Phys. Chem. Solids* **64**, 863 (2003).

<sup>13</sup>M. J. Mehl, Aarón Aguayo, L. L. Boyer, and R. de Coss, *Phys. Rev. B* **70**, 014105 (2004).

<sup>14</sup>Note that the LS-fcc global minimum does not represent the lowest energy if spin noncollinear orientations are allowed. LS-fcc and noncollinear spin configurations have been studied previously in, e.g., Elisabeth Sjöstedt and Lars Nordström, *Phys. Rev. B* **66**, 014447 (2002); S. Shallick, A. E. Kissavos, S. Sharma, and V. Meded, *ibid.* **73**, 104443 (2006), but are not be discussed here.

<sup>15</sup>See, e.g., P. Larson, I. I. Mazin, and D. J. Singh, *Phys. Rev. B* **69**, 064429 (2004).

<sup>16</sup>By high-spin and low-spin notations we mean, in fact, the states of iron atoms (even in compounds) because the magnetic moment of palladium atoms is low in any case.

<sup>17</sup>D. B. Laks, L. G. Ferreira, S. Froyen, and A. Zunger, *Phys. Rev. B* **46**, 12587 (1992); A. Zunger, L. Wang, G. Hart, and M. Sanati, *Modell. Simul. Mater. Sci. Eng.* **10**, 685 (2002).

- <sup>18</sup>See also a recent alternative justification of the constrained (“penalized”) least-square minimization in E. Cockayne and A. van de Walle, *Phys. Rev. B* **81**, 012104 (2010).
- <sup>19</sup>G. L. W. Hart, V. Blum, M. J. Walorski, and A. Zunger, *Nat. Mater.* **4**, 167 (2005).
- <sup>20</sup>V. Blum and A. Zunger, *Phys. Rev. B* **70**, 155108 (2004); V. Blum, G. L. W. Hart, M. J. Walorski, and A. Zunger, *ibid.* **72**, 165113 (2005).
- <sup>21</sup>S. V. Barabash, V. Blum, S. Müller, and A. Zunger, *Phys. Rev. B* **74**, 035108 (2006).
- <sup>22</sup>V. Blum and A. Zunger, *Phys. Rev. B* **69**, 020103 (2004).
- <sup>23</sup>Z. W. Lu, B. M. Klein, and A. Zunger, *Superlattices Microstruct.* **18**, 161 (1995).
- <sup>24</sup>Z. W. Lu, D. B. Laks, S.-H. Wei, and A. Zunger, *Phys. Rev. B* **50**, 6642 (1994).
- <sup>25</sup>Y. Wang and J. P. Perdew, *Phys. Rev. B* **44**, 13298 (1991).
- <sup>26</sup>S. H. Vosko, L. Wilk, and M. Nusair, *Can. J. Phys.* **58**, 1200 (1980).
- <sup>27</sup>G. Kresse and J. Furthmüller, *Comput. Mater. Sci.* **6**, 15 (1996); *Phys. Rev. B* **54**, 11169 (1996); G. Kresse and D. Joubert, *Phys. Rev. B* **59**, 1758 (1999).
- <sup>28</sup>M. Asato, A. Settels, T. Hoshino, T. Asada, S. Blügel, R. Zeller, and P. H. Dederichs, *Phys. Rev. B* **60**, 5202 (1999).
- <sup>29</sup>V. L. Moruzzi, J. F. Janak, and A. R. Williams, *Calculated Electronic Properties of Metals* (Pergamon, New York, 1978).
- <sup>30</sup>H. C. Herper, E. Hoffmann, and P. Entel, *Phys. Rev. B* **60**, 3839 (1999).
- <sup>31</sup>Y. Chen, T. Atago, and T. Mohri, *J. Phys.: Condens. Matter* **14**, 1903 (2002); T. Mohri and Y. Chen, *J. Alloys Compd.* **383**, 23 (2004); T. Mohri and Y. Chen, *Mater. Trans.* **45**, 1478 (2004); Y. Chen, S. Iwata, and T. Mohri, *Mater. Sci. Forum* **475–479**, 3127 (2005).
- <sup>32</sup>Y. Mishin, M. J. Mehl, and D. A. Papaconstantopoulos, *Acta Mater.* **53**, 4029 (2005).
- <sup>33</sup>C. Kittel, *Introduction to Solid State Physics*, 8th ed. (Wiley, New York, 2005).
- <sup>34</sup>P. Villars and L. D. Calvert, *Pearson’s Handbook of Crystallographic Data for Intermetallic Phases*, 2nd ed. (ASM, Metals Park, OH, 1991).
- <sup>35</sup>A. N. Timoshevskii, B. Z. Yanchitsky, and A. S. Bakai, *Low Temp. Phys.* **30**, 469 (2004).
- <sup>36</sup>J. P. Perdew, K. Burke, and M. Ernzerhof, *Phys. Rev. Lett.* **77**, 3865 (1996); **78**, 1396 (1997).
- <sup>37</sup>S. C. Abrahams, L. Guttman, and J. S. Kasper, *Phys. Rev.* **127**, 2052 (1962).
- <sup>38</sup>R. R. Duplessis, R. A. Stern, and J. M. MacLaren, *J. Appl. Phys.* **95**, 6589 (2004).
- <sup>39</sup>C. B. Alcock and A. Kubik, *Acta Metall.* **17**, 437 (1969); R. Hultgren, P. D. Desai, D. T. Hawkins, M. Gleiser, and K. K. Kelley, *Selected Values of the Thermodynamic Properties of Binary Alloys* (ASM, Metals Park, OH, 1973); O. Kubaschewski, C. B. Alcock, and P. J. Spencer, *Materials Thermochemistry* (Pergamon Press, Oxford, 1993).
- <sup>40</sup>M. Elzain, A. Al Rawas, A. Yousif, A. Gismelseed, A. Rais, I. Al Omari, and H. Widatallah, *Phys. Status Solidi C* **1**, 1796 (2004).
- <sup>41</sup>M. H. P. Corrêa, W. H. Schreiner, J. E. Schmidt, P. J. Viccaro, and A. Vasquez, *J. Phys. F* **15**, 1779 (1985).
- <sup>42</sup>J. W. Cable, E. O. Wollan, and W. C. Koehler, *Phys. Rev.* **138**, A755 (1965); *Magnetic Properties of Metals*, edited by H. P. J. Wijn (Springer, Berlin, 1991).
- <sup>43</sup>E. M. Lifshitz, *J. Phys. (USSR)* **6**, 61, 251 (1942); L. D. Landau and E. M. Lifshitz, *Course of Theoretical Physics*, Vol. 5 (Pergamon, Oxford, 1980).
- <sup>44</sup>A. G. Khachatryan, *Prog. Mater. Sci.* **22**, 1 (1978); *Theory of Structural Transformations in Solids* (John Wiley and Sons, New York, 1983).
- <sup>45</sup>A. P. Cracknell, *J. Phys. C* **6**, 826 (1973).
- <sup>46</sup>V. N. Bugaev and R. V. Chepulskii, *Phys. Status Solidi B* **192**, 9 (1995).
- <sup>47</sup>*International Tables for Crystallography*, edited by T. Hahn, Vol. A (D. Reidel, Dordrecht, 1983).
- <sup>48</sup>C. B. Alcock and A. Kubik, *Acta Metall.* **17**, 437 (1969); R. Hultgren, P. D. Desai, D. T. Hawkins, M. Gleiser, and K. K. Kelley, *Selected Values of the Thermodynamic Properties of Binary Alloys* (ASM, Metals Park, OH, 1973); O. Kubaschewski, C. B. Alcock, and P. J. Spencer, *Materials Thermochemistry* (Pergamon Press, Oxford, 1993).
- <sup>49</sup>J. Tomiska, *Z. Metallkd.* **80**, 888 (1989).
- <sup>50</sup>T. Mehaddene, *J. Phys.: Condens. Matter* **17**, 485 (2005).
- <sup>51</sup>T. Mehaddene, J. M. Sanchez, R. Caudron, M. Zemirli, and V. Pierron-Bohnes, *Eur. Phys. J. B* **41**, 207 (2004).
- <sup>52</sup>M. Sanati, L. G. Wang, and A. Zunger, *Phys. Rev. Lett.* **90**, 045502 (2003).
- <sup>53</sup>V. Ozoliņš, C. Wolverton, and A. Zunger, *Phys. Rev. B* **57**, 6427 (1998); **58**, R5897 (1998).
- <sup>54</sup>R. V. Chepulskii and S. Curtarolo, *Appl. Phys. Lett.* **99**, 261902 (2011).
- <sup>55</sup>See Supplemental Material at <http://link.aps.org/supplemental/10.1103/PhysRevB.85.144201> for convergence tests (k-point, energy cutoff, and pseudopotentials), atomic coordinates of all the structures calculated in DFT, filtering procedures, and constrained pair fitting.
- <sup>56</sup>L. G. Ferreira, S.-H. Wei, and A. Zunger, *Int. J. Supercomput. Appl.* **5**, 34 (1991).
- <sup>57</sup>Note that the structures representing the convex hull may be different from the structures corresponding to minimum formation energy at fixed compositions. This is the case when the energy of phase segregation at given composition is lower than the energy of any structure with the same stoichiometric composition. For an exhaustive search, the convex hull identifies all the ground state structures. (We do not use the term “ground state” to refer to phase-separated mixtures.)
- <sup>58</sup>To avoid confusion, please note that the true DFT ground states do not change throughout the CE iterations, but the DFT convex hull does. Indeed, whether or not a given structure is a ground state of a given Hamiltonian is a fact independent of the search procedure. In contrast, members of a convex hull determined from a finite set of energies may change if other competing energies are added to the set.
- <sup>59</sup>R. J. Weiss and K. J. Tauer, *Phys. Rev.* **102**, 1490 (1956).
- <sup>60</sup>T. B. Massalski and D. E. Laughlin, *Calphad* **33**, 3 (2009).
- <sup>61</sup>A. V. Ruban, P. A. Korzhavyi, and B. Johansson, *Phys. Rev. B* **77**, 094436 (2008); M. Rahaman, A. V. Ruban, A. Mookerjee, and B. Johansson, *ibid.* **83**, 054202 (2011).